

# Radical chemistry in the Pearl River Delta: observations and modeling of OH and HO<sub>2</sub> radicals in Shenzhen 2018

Xinping Yang<sup>1,2</sup>, Keding Lu<sup>1,2,\*</sup>, Xuefei Ma<sup>1,2</sup>, Yue Gao<sup>1,2</sup>, Zhaofeng Tan<sup>3</sup>, Haichao Wang<sup>4</sup>, Xiaorui Chen<sup>1,2</sup>, Xin Li<sup>1,2</sup>, Xiaofeng Huang<sup>5</sup>, Lingyan He<sup>5</sup>, Mengxue Tang<sup>5</sup>, Bo Zhu<sup>5</sup>, Shiyi Chen<sup>1,2</sup>, Huabin Dong<sup>1,2</sup>, Limin Zeng<sup>1,2</sup>, Yuanhang Zhang<sup>1,2,\*</sup>

<sup>1</sup>State Key Joint Laboratory of Environmental Simulation and Pollution Control, College of Environmental Sciences and Engineering, Peking University, Beijing, China

<sup>2</sup>State Environmental Protection Key Laboratory of Atmospheric Ozone Pollution Control, Peking University, Beijing, China

<sup>3</sup>Institute of Energy and Climate Research, IEK-8: Troposphere, Forschungszentrum Juelich GmbH, Juelich, Germany

<sup>4</sup>School of Atmospheric Sciences, Sun Yat-Sen University, Zhuhai, China

<sup>5</sup>Laboratory of Atmospheric Observation Supersite, School of Environment and Energy, Peking University Shenzhen Graduate School, Shenzhen, China

Correspondence to: Keding Lu ([k.lu@pku.edu.cn](mailto:k.lu@pku.edu.cn)), Yuanhang Zhang ([yhzhang@pku.edu.cn](mailto:yhzhang@pku.edu.cn))

**Abstract.** The ambient radical concentrations were measured continuously by laser-induced fluorescence during the STORM (STudy of the Ozone foRmation Mechanism) campaign at the Shenzhen site, located in the Pearl River Delta in China, in the autumn of 2018. The diurnal maxima were  $4.5 \times 10^6 \text{ cm}^{-3}$  for OH radicals and  $4.2 \times 10^8 \text{ cm}^{-3}$  for HO<sub>2</sub> radicals (including an estimated interference of 23%-28% from RO<sub>2</sub> radicals during the daytime), respectively. The state-of-the-art chemical mechanism underestimated the observed OH concentration, similar to the other warm-season campaigns in China. The OH underestimation was attributable to the missing OH sources, which can be explained by the X mechanism. Good agreement between the observed and modeled OH concentrations was achieved when an additional numerical X equivalent to 0.1 ppb NO concentrations was added into the base model. The isomerization mechanism of RO<sub>2</sub> derived from isoprene contributed approximately 7% to the missing OH production rate and the oxidation of isoprene oxidation products (MACR and MVK) had no significant impact on the missing OH sources, demonstrating further exploration of unknown OH sources is necessary. A significant HO<sub>2</sub> heterogeneous uptake was found in this study, with an effective uptake coefficient of 0.3. The model with the HO<sub>2</sub> heterogeneous uptake can simultaneously reproduce the OH and HO<sub>2</sub> concentrations when the amount of X changed from 0.1 to 0.25 ppb. The RO<sub>x</sub> primary production rate was dominated by photolysis reactions, in which the HONO, O<sub>3</sub>, HCHO, and carbonyls photolysis accounted for 29%, 16%, 16%, and 11% during the daytime, respectively. The RO<sub>x</sub> termination rate was dominated by the reaction of OH + NO<sub>2</sub> in the morning, and thereafter the radical self-combination gradually became the major sink of RO<sub>x</sub> in the afternoon. As the sum of the respective oxidation rates of the pollutants via reactions with oxidants, the atmospheric oxidation capacity was evaluated, with a peak of 11.8 ppb h<sup>-1</sup> around noontime. The ratio of  $P(\text{O}_3)_{\text{net}}$  to  $\text{AOC}_{\text{VOCs}}$ , which indicates the yield of net ozone production from VOCs oxidation, trended to increase and then decrease as the NO concentration increased. The median ratios ranged within 1.0-4.5, with the maximum existing when the NO

34 concentration was approximately 1 ppb. The nonlinear relationship between the yield of net ozone production from VOCs  
35 oxidation and NO concentrations demonstrated that optimizing the NO<sub>x</sub> and VOCs control strategies is critical to controlling  
36 ozone pollution effectively in the future.

## 37 **1 Introduction**

38 Severe ambient ozone (O<sub>3</sub>) pollution is one of China's most significant environmental challenges (Shu et al., 2020;Li et al.,  
39 2019;Wang et al., 2020;Ma et al., 2019b;Wang et al., 2017a). Despite the reduction in emissions of O<sub>3</sub> precursors, O<sub>3</sub>  
40 concentration is increasing, especially in urban cities. The O<sub>3</sub> average trends for the focus megacity clusters are 3.1 ppb a<sup>-1</sup>,  
41 2.3 ppb a<sup>-1</sup>, 0.56 ppb a<sup>-1</sup>, and 1.6 ppb a<sup>-1</sup> for North China Plain (NCP), Yangtze River Delta (YRD), Pearl River Delta (PRD),  
42 and Szechwan Basin (SCB), respectively (Li et al., 2019). The nonlinearity between O<sub>3</sub> and precursors illustrates that exploring  
43 the cause of O<sub>3</sub> production is necessary. The tropospheric O<sub>3</sub> is only generated in the photolysis of nitrogen dioxide (NO<sub>2</sub>)  
44 which is produced as the by-product within the radical cycling. Thus, the investigation of radical chemistry is critical to  
45 controlling secondary pollution.

46 Hydroxyl radicals (OH), the dominant oxidant, control the atmospheric oxidation capacity (AOC) in the troposphere. The  
47 OH radicals convert primary pollutants to secondary pollutants and are simultaneously transformed into peroxy radicals (HO<sub>2</sub>  
48 and RO<sub>2</sub>). Within the interconvert of RO<sub>x</sub> (= OH, HO<sub>2</sub>, and RO<sub>2</sub>), secondary pollutants are generated, and thus the further  
49 exploration of radical chemistry is significant. The radical closure experiment, an effective indicator for testing our  
50 understanding of radical chemistry, has been conducted since the central role of OH radicals was recognized in the 1970s (Levy,  
51 1971;Hofzumahaus et al., 2009). The underestimation of OH radicals in environments characterized by low nitrogen oxides  
52 (NO) and high volatile organic compounds (VOCs) has been identified (Lu et al., 2013;Lu et al., 2012;Tan et al., 2017;Tan et  
53 al., 2019;Yang et al., 2021;Hofzumahaus et al., 2009;Lelieveld et al., 2008;Whalley et al., 2011). New radical mechanisms  
54 involving unclassical OH regeneration have been proposed, mainly including Leuven Isoprene Mechanism (LIM) and X  
55 mechanism (Peeters and Muller, 2010;Peeters et al., 2014;Peeters et al., 2009;Hofzumahaus et al., 2009). The LIM which has  
56 been integrated into the current radical mechanism is still insufficient to explain the OH missing sources. The X mechanism  
57 was identified several times, but the amount of the numerical species, X, varied in different environments, and the nature of X  
58 is still unknown (Hofzumahaus et al., 2009;Lu et al., 2013;Lu et al., 2012;Tan et al., 2017;Tan et al., 2019;Yang et al., 2021;Ma  
59 et al., 2022a). Therefore, further exploration of radical regeneration sources is necessary.

60 Due to the strong photochemistry influenced by high temperatures and strong radiation, severe O<sub>3</sub> pollution appeared to  
61 occur in YRD and PRD, especially in PRD (Ma et al., 2019b;Wang et al., 2017a). Radicals, the dominant oxidant in the  
62 troposphere, have been measured during warm seasons in NCP (Yufa 2006, Wangdu 2014, and Beijing 2016), YRD (Taizhou  
63 2018), SCB (Chengdu 2019), and PRD (Backgarden 2006, and Heshan 2014) in China (Lu et al., 2013;Lu et al., 2012;Tan et

64 al., 2017;Tan et al., 2019;Yang et al., 2021;Tan et al., 2021;Ma et al., 2022a). The radical observations in PRD, where the cities  
65 are suffering from severe O<sub>3</sub> pollution, have not been conducted since 2014, and thus the oxidation capacity here has not been  
66 clear in recent years. Therefore, we carried out a continuous comprehensive field campaign (STudy of the Ozone foRmation  
67 Mechanism - STORM) involving radical observations in Shenzhen, one of the megacities in PRD, in the autumn of 2018.  
68 Overall, the following will be reported in this study.

- 69 (1) The observed radical concentrations, and the comparison between the radical observations and simulations.
- 70 (2) The exploration of the unclassical OH regeneration sources based on the experimental budget.
- 71 (3) The sources and sinks of RO<sub>x</sub> radicals.
- 72 (4) The evaluation of the atmospheric oxidation capacity.

## 73 2 Methodology

### 74 2.1 Measurement site and instrumentation

75 The STORM campaign was conducted from September to October 2018 in Peking University Shenzhen Graduate School  
76 (22.60 deg N, 113.97 deg E), in the west of Shenzhen, Guangdong province. As shown in Fig. 1, this site, which belongs to  
77 the urban site, is located in the university town, and is surrounded by residential and commercial areas. The northwest of the  
78 site is close to the Shenzhen Wildlife Park, and the northeast is close to the Xili Golf Club (Yu et al., 2020). The Tanglang  
79 Mountain Park with active biogenic emissions is located about 1 km southeast of the site. Overall, this site has no significant  
80 local pollution sources nearby, but can represent the urban pollution characteristics (Huang et al., 2012a;Huang et al.,  
81 2012b;Gao et al., 2018).

82



83

84 Figure 1: Geographical location and surrounding environmental conditions of the measurement site in the STORM campaign (The

85 maps are from <https://map.baidu.com>).

86 Most instruments were set up on the top of a four-story academic building (about 20 m). Besides HO<sub>x</sub> radicals measured by  
87 the Peking University-Laser Induced Fluorescence system (PKU-LIF) (see the details in Sect. 2.2), a comprehensive set of  
88 trace gases was conducted to support the exploration of radical chemistry, including meteorological parameters (temperature,  
89 pressure, relative humidity, *etc.*), photolysis frequency, OH reactivity ( $k_{\text{OH}}$ ) and the trace gases (NO, NO<sub>2</sub>, O<sub>3</sub>, VOCs, *etc.*).  $k_{\text{OH}}$   
90 was measured by the Laser flash Photolysis-Laser Induced Fluorescence system (LP-LIF). Most of the inorganic trace gases  
91 (O<sub>3</sub>, CO, NO, NO<sub>2</sub>, and SO<sub>2</sub>) were simultaneously measured by two sets of instruments, and good agreement was achieved  
92 within the uncertainty. VOCs species (alkanes, alkenes, aromatics, isoprene, and oxygenated VOCs (OVOCs)) were measured  
93 using a gas chromatograph following a mass spectrometer (GC-MS). In addition, HONO and HCHO were measured as well.  
94 Table S1 in the Supplementary Information presents the experimental details of the meteorological and chemical parameters  
95 during this campaign.

## 96 2.2 The OH and HO<sub>2</sub> measurements

97 The OH and HO<sub>2</sub> radicals were measured by PKU-LIF based on the fluorescence assay by gas expansion (FAGE) technique.  
98 The principle has been reported in previous studies, and only a brief description of the instrument is presented here. Further  
99 detailed information on the instrument can be found in previous studies (Heard and Pilling, 2003;Fuchs et al., 2008;Holland  
100 et al., 1995;Hofzumahaus et al., 1996;Fuchs et al., 2011).

101 In principle, OH resonance fluorescence is released in the OH excitation by a 308 nm pulsed laser, and then OH radicals are  
102 detected directly. HO<sub>2</sub> radicals are converted into OH via NO, and then they are detected. The system contains a laser module  
103 and a detection module. Ambient air was drawn into two independent, parallel, low-pressure (3.5 mBar) cells through two  
104 parallel nozzles with 0.4 mm diameter pinhole. The OH radicals are excited into resonance fluorescence in the OH detection  
105 cell and detected by micro-channel plate detectors (MCP). In the HO<sub>2</sub> detection cell, NO is injected and converts HO<sub>2</sub> to OH  
106 radicals, and then OH radicals are excited by the laser and release resonance fluorescence. Besides, an OH reference cell in  
107 which a large OH concentration is generated by pyrolysis of water vapor on a hot filament is applied to automatically correct  
108 the laser wavelength.

109 Owing to the failure of the reference cell in this campaign, the NO mixing ratios injected into the HO<sub>2</sub> detection cell were  
110 set to be higher than those in other campaigns in China because the HO<sub>2</sub> cell needed to be used as a reference cell to correct  
111 laser wavelength. In this campaign, NO mixing ratios were switched between 25 ppm (low NO mode) and 50 ppm (high NO  
112 mode). We calculated the HO<sub>2</sub>-to-OH conversion efficiencies under the two different NO concentrations by calibrating the  
113 PKU-LIF system. HO<sub>2</sub>-to-OH conversion efficiencies in low NO mode ranged within 80%-95%, while those in high NO mode  
114 reached 100%, demonstrating that the high NO concentration is sufficient to achieve the complete HO<sub>2</sub>-to-OH conversion and  
115 thus the HO<sub>2</sub> measurement was affected by RO<sub>2</sub> radicals. Prior studies have reported the relative detection sensitivities ( $\alpha_{\text{RO}_2}$ )

116 for the major RO<sub>2</sub> species, mainly from alkenes, isoprene and aromatics. Fuchs et al. (2011) reported that the relative RO<sub>2</sub>  
117 detection sensitivities are approximately constant when the NO concentration is so high that HO<sub>2</sub> conversion in the detection  
118 is nearly complete. Thus, when the HO<sub>2</sub>-to-OH conversion efficiencies reach 100%, the relative RO<sub>2</sub> detection sensitivities  
119 reported by Fuchs et al. (2011) and Lu et al. (2012) can be used for the correction of HO<sub>2</sub> concentrations (Fuchs et al., 2011; Lu  
120 et al., 2012; Lu et al., 2013). Herein, only the HO<sub>2</sub> observations in high NO mode were chosen and they were denoted as [HO<sub>2</sub>\*],  
121 which was the sum of the true HO<sub>2</sub> concentration and a systematic bias from the mixture of RO<sub>2</sub> species *i* which were detected  
122 with different relative sensitivities  $\alpha_{RO_2}^i$ , as shown in Eq. (1) (Lu et al., 2012). The true HO<sub>2</sub> concentration was difficult to be  
123 calculated because the observed concentrations of RO<sub>2</sub> and their speciation were not available. Herein, we simulated the HO<sub>2</sub>  
124 and HO<sub>2</sub>\* concentrations by the model, and the RO<sub>2</sub> interference yields which were used for correction were the modeled  
125 values reported by Lu et al. (2012) in the PRIDE-PRD2006 campaign in which the HO<sub>2</sub>-to-OH conversion efficiencies also  
126 reached 100% due to the injection of pure NO in the HO<sub>2</sub> detection cell. The interference from RO<sub>2</sub> radicals was estimated to  
127 be the difference between the modeled HO<sub>2</sub> and HO<sub>2</sub>\* concentrations. Overall, the measurement uncertainties of OH and HO<sub>2</sub>\*  
128 radicals were 11% and 15%, respectively, as shown in Table S1 in the Supplementary Information.

$$129 \quad [HO_2^*] = [HO_2] + \sum(\alpha_{RO_2}^i \times [RO_2]_i) \quad (1)$$

130 Additionally, prior studies reported that OH measurement might be affected by the potential interference, when the sampled  
131 air contains ozone, alkenes and BVOCs (Mao et al., 2012; Fuchs et al., 2016; Novelli et al., 2014), indicating the environmental  
132 conditions are important to the production of interference. The pre-injector is usually used to test the potential OH interference,  
133 and has been applied to our PKU-LIF system to quantify the possible interferences for several campaigns, including the  
134 campaigns conducted at the Wangdu, Heshan, Huairou, Taizhou and Chengdu sites (Tan et al., 2017; Tan et al., 2019; Tan et al.,  
135 2018; Yang et al., 2021; Ma et al., 2022b). No significant internal interference was found in the prior studies, demonstrating the  
136 accuracy of the PKU-LIF system has been determined for several times. Moreover, to further explore the potential interference  
137 in this campaign, we compared the major environmental conditions, especially O<sub>3</sub>, alkenes and isoprene, between Shenzhen  
138 and Wangdu sites, as shown in the Supplementary Information. The results indicated that the environmental condition in  
139 Shenzhen was less conducive to generating interference than that in Wangdu, and the details were presented in the  
140 Supplementary Information. Besides the environmental conditions, the prior studies reported that the product of the reaction  
141 of RO<sub>2</sub> with OH, trioxides (ROOOH), might lead to an OH interference signal. The reactions of RO<sub>2</sub> radicals with OH radicals  
142 might be competitive with other sinks for RO<sub>2</sub> radicals (Fittschen, 2019; Fittschen et al., 2019; Berndt et al., 2022). Fittschen et  
143 al. (2019) reported that the OH interference signals might come from the ROOOH heterogeneous decomposition on the walls  
144 of the FAGE cell or the entrance nozzle, but they also noted that the ROOOH interference is highly dependent on the design  
145 and measurement conditions of different FAGE instruments. Therefore, we integrated the reactions of the ROOOH production  
146 and destruction into the base model herein, with the ROOOH production rate constant of  $1.5 \times 10^{-10} \text{ cm}^3 \text{ s}^{-1}$  and the destruction

147 rate constant of  $10^{-4} \text{ s}^{-1}$  (the details are presented in the Supplementary Information) (Fittschen et al., 2019). Figure. S1 (a)  
148 presents the modeled ROOOH concentrations during this campaign, with a maximum of about  $4.4 \times 10^9 \text{ cm}^{-3}$ . The correlation  
149 of the modeled ROOOH concentrations and the ratios of OH observations to OH simulations, and the correlation of the  
150 modeled ROOOH concentrations and the difference between OH observations and simulations both demonstrated that no  
151 significant relevance between ROOOH and the underestimation of OH radicals, as shown in Fig. S1 (b-c). Additionally, the  
152 ROOOH values modeled in our another campaign (Taizhou, 2018) were comparable to or even slightly higher than the  
153 simulations in this study, and the chemical modulation tests in Taizhou confirmed the ROOOH is not a significant OH  
154 interference in our PKU-LIF system (Ma et al., 2022b). Overall, the OH interference during this campaign was negligible  
155 according to the analysis of the behavior of PKU-LIF system in previous campaigns, the comparison of environmental  
156 conditions between this campaign and Wangdu campaign, and the exploration of the impact of ROOOH on the discrepancy of  
157 OH observations and simulations. However, we should acknowledge that the unmeasured interference might have an effect on  
158 radical measurement. More precise chemical modulation tests are needed in the future.

159

### 160 **2.3 Closure experiment**

161 As an effective tool to explore the atmospheric radical chemistry, the radical closure experiment can investigate the state-of-  
162 the-art chemical mechanism because of the extremely short lifetime of radicals (Stone et al., 2012; Lu et al., 2019). A zero-  
163 dimensional box model was used to conduct the radical closure experiment, and the overall framework was reported by Lu et  
164 al. (2019). In this work, we conducted the radical closure experiment based on the Regional Atmospheric Chemical Mechanism  
165 updated with the latest isoprene chemistry (RACM2-LIM1), as Tan et al. (2017) described in detail. The model was constrained  
166 by the measured meteorological, photolysis frequency, and the critical chemical parameters (CO, NO, NO<sub>2</sub>, VOCs, *etc.*). The  
167 H<sub>2</sub> and CH<sub>4</sub> mixing ratios were set to 550 ppb and 1900 ppb, respectively. The model was operated in time-dependent mode  
168 with a 5-min time resolution, and a 2-d spin-up time was to make the unconstrained species approach the steady state relative  
169 to the constrained species.

170 As Lu et al. (2012) described, there are two types of radical closure experiment. One is the comparison of observed and  
171 modeled radical concentrations, and the other is the comparison of radical production and destruction rates. The most  
172 significant difference between the above is that the latter is conducted with the observed radical concentrations and  $k_{\text{OH}}$   
173 constrained. The comparison of radical production and destruction rates, which is also called radical experimental budget, can  
174 test the accuracy of the state-of-the-art chemistry mechanisms based on the equivalent relationship between the radical  
175 production and destruction rates. The production rates of OH, HO<sub>2</sub>, and RO<sub>2</sub> radicals are quantified from all the known sources.  
176 The destruction rates of HO<sub>2</sub> and RO<sub>2</sub> radicals are the sum of the known sinks, while the OH destruction rate can be directly  
177 calculated as the product of the observed OH concentrations and the observed  $k_{\text{OH}}$  (Tan et al., 2019; Yang et al., 2021). The OH

178 destruction rate is the total sinks of OH radicals because of the direct  $k_{OH}$  observation, and thus the discrepancy between the  
179 OH destruction and production rates denotes the missing OH sources. The detailed reactions and the reaction rate constants  
180 related to OH, HO<sub>2</sub>, and RO<sub>2</sub> radicals can be found in Tan et al. (2019) and Yang et al. (2021).

## 181 2.4 AOC evaluation

182 The life time of the trace gases is controlled not only by the oxidant concentration but also by its second-order rate constant,  
183 so the atmospheric oxidation capacity (AOC) proposed by Geyer et al. (2001) is most suitable to evaluate the relative  
184 importance of each oxidant (Elshorbany et al., 2009). AOC is the core driving force of complex air pollution, and determines  
185 the removal rate of trace gases and the production rates of secondary pollutants (Liu et al., 2021). As an effective indicator for  
186 atmospheric oxidation intensity, the evaluation of AOC can provide crucial information on the atmospheric composition of  
187 harmful and climate forcing species (Elshorbany et al., 2009). AOC is defined as the sum of the respective oxidation rates of  
188 the pollutants via reactions with oxidants (Elshorbany et al., 2009;Geyer et al., 2001;Zhu et al., 2020). According to the  
189 definition of AOC, it can be calculated by the Eq. (2).

$$190 \text{ AOC} = \sum_i k_{Y_i}[Y_i][X] \quad (2)$$

191 where  $Y_i$  are the pollutants (CO, CH<sub>4</sub>, and VOCs),  $X$  are the main atmospheric oxidants (OH, O<sub>3</sub>, NO<sub>3</sub>), and  $k_{Y_i}$  is the bi-  
192 molecular rate constant for the reaction of  $Y_i$  with  $X$ . AOC includes all combination of pollutants  $Y$  and oxidants  $X$ . The  
193 higher AOC, the higher removal rate of the atmospheric pollutants, and thus the higher production rate of secondary pollutants  
194 (Yang et al., 2020b). Simultaneous measurements of OH and the key trace gases are available in the study. NO<sub>3</sub> concentration  
195 could be simulated by the box model with the observed parameters constrained.

## 196 3. Results

### 197 3.1 Meteorological and chemical conditions

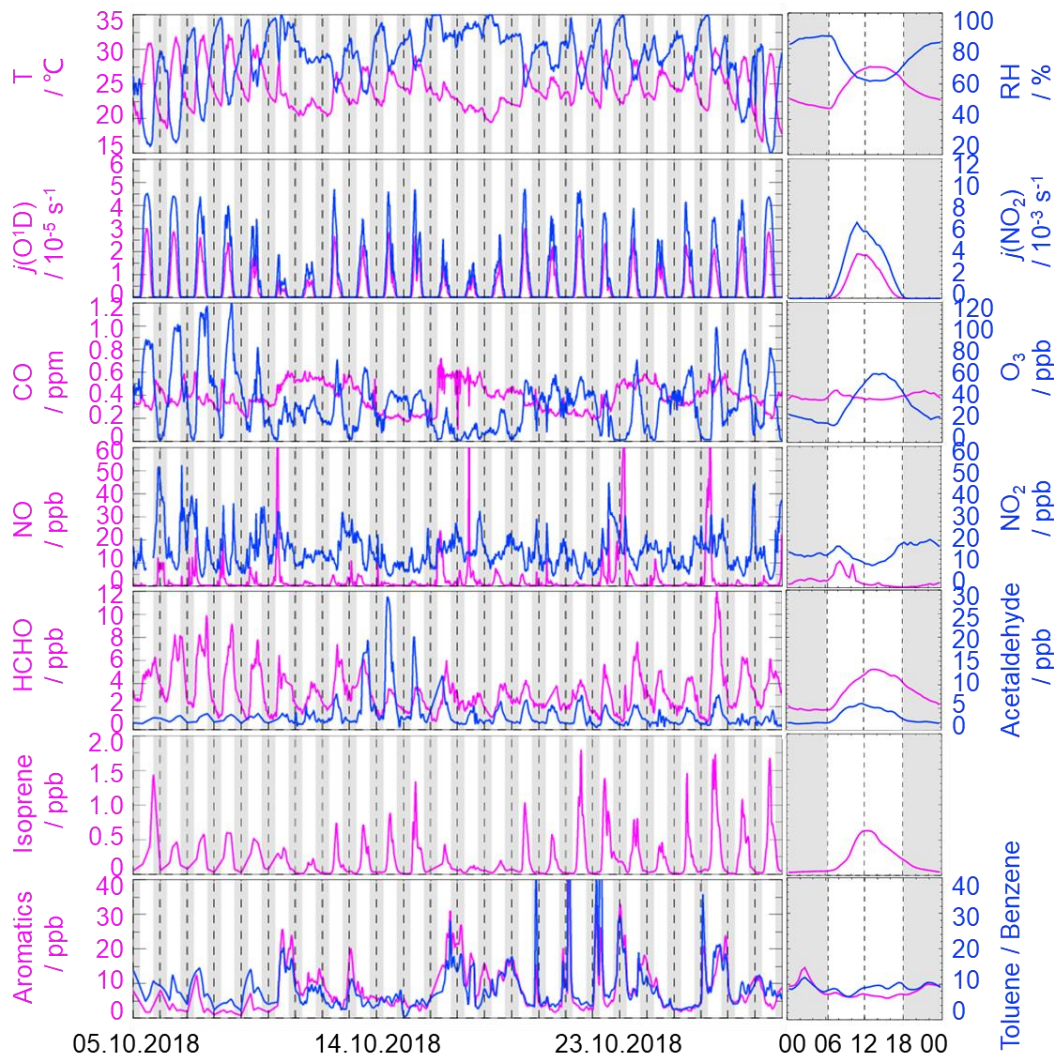
198 Figure 2 gives an overview of the meteorological and chemical parameters from 05 October to 28 October 2018, when OH  
199 and HO<sub>2</sub> radicals were measured. The diurnal variations of the temperature (T), relative humidity (RH),  $j(\text{O}^1\text{D})$ , and  $j(\text{NO}_2)$   
200 followed a regular pattern from day to day. The overall meteorological conditions were characterized by high temperature  
201 (about 20~30 °C), high relative humidity (60~80%), and intensive radiation with  $j(\text{O}^1\text{D})$  up to  $2.0 \times 10^{-5} \text{ s}^{-1}$  and  $j(\text{NO}_2)$  up to  
202  $6.0 \times 10^{-3} \text{ s}^{-1}$ . The relative humidity and photolysis-frequency in this autumn campaign were similar to those in the summer  
203 campaign conducted in Chengdu (Yang et al., 2021). The temperature in this campaign was lower than that in Chengdu, but  
204 similar to that in the autumn campaign in Heshan located in PRD as well (Tan et al., 2019;Yang et al., 2021).

205 The concentration of CO showed a weak diurnal variation, indicating there was the non-obvious accumulation of  
206 anthropogenic emissions on a regional scale. NO concentration peaked at 12 ppb during morning rush hour when the traffic

207 emission was severe, and thereafter, O<sub>3</sub> concentration started to increase with the decreasing of NO concentration. The maxima  
208 of O<sub>3</sub> hourly concentration were high up to 120 ppb. According to the updated National Ambient Air Quality Standard of China  
209 (GB3095-2012), O<sub>3</sub> concentration exceeded the Class-II limit values (hourly averaged limit 93 ppb) on several days (6, 7, 8,  
210 and 26 October) when the environmental condition was characterized by high temperature and low relative humidity. NO<sub>2</sub>  
211 concentration was high at night because of the titration effect of O<sub>3</sub> with NO.

212 Along with the high O<sub>3</sub> concentration on 6, 7, 8, and 26 October, high HCHO concentration was also recorded during the  
213 corresponding periods, indicating HCHO was mainly produced as secondary pollutants because of the active photochemistry  
214 in this campaign. Isoprene, which is mostly derived from biogenic emissions and mainly affected by temperature, peaked  
215 around noontime. Tan et al. (2019) reported the median concentration of HCHO and isoprene concentrations were 6.8 ppb and  
216 0.6 ppb during 12:00-18:00 at Heshan site. Similarly, the median concentration of HCHO and isoprene concentrations in this  
217 study were 4.9 ppb and 0.4 ppb during the corresponding periods, respectively. As a proxy for traffic intensity, the toluene to  
218 benzene ratio (T/B), which is below 2, means the traffic emissions are the major sources of VOCs (Brocco et al., 1997). In this  
219 campaign, the T/B gradually dropped from 07:00 until it reached the minimum value at 09:00, indicating traffic emission  
220 contributed more to VOCs during morning rush hour than during other periods. However, the T/B values, which varied within  
221 a range of 7-12, were above 2, and thus VOCs emission during this campaign was mainly from other sectors such as those  
222 involving solvent evaporation.





223

224

**Figure 2: Timeseries and diurnal profiles of the observed meteorological and chemical parameters in the STORM campaign. The grey areas denote nighttime.**

225

226

227

228

229

230

231

232

233

234

235

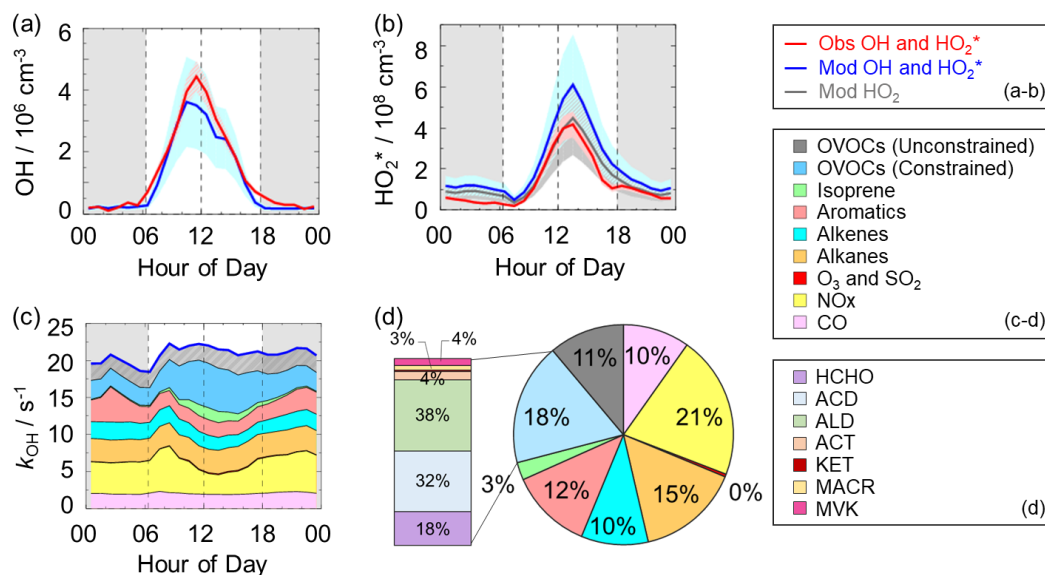
Moreover, we compared the environmental conditions between the Backgarden (rural site), Heshan (suburban site), and Shenzhen (urban site) campaigns conducted in PRD in Table S3 in the Supplementary Information. No significant discrepancy in temperature was found in the Shenzhen and Heshan campaigns, which were both conducted in autumn. The temperature in the Backgarden campaign conducted in summer was higher than those in Shenzhen and Heshan. The relative humidity in Shenzhen and Backgarden was higher than that in Heshan. Compared to the chemical conditions in the Heshan campaign conducted in autumn as well, the concentrations of CO, NO, NO<sub>2</sub>, HONO, alkenes, aromatics, and HCHO in Shenzhen were lower, which might be because there were no significant local pollution sources nearby at the Shenzhen site although it was an urban site. However, the concentration of O<sub>3</sub> which is the typical secondary pollutant in Shenzhen was higher than that in Heshan. Compared to the environmental conditions in Heshan, the higher O<sub>3</sub> concentration in Shenzhen might benefit from the weather condition which was characterized by the stronger solar radiation and slightly higher temperatures.

### 236 3.2 Observed and modeled OH and HO<sub>2</sub> radicals

237 The OH and HO<sub>2</sub> radicals were measured during 05-28 October 2018. The timeseries of the observed and modeled HOx  
238 concentrations are displayed in Fig. S2 (a-b) in the Supplementary Information. Data gaps were caused by the rain, calibration,  
239 and maintenance. The daily maxima of the observed OH and HO<sub>2</sub>\* concentrations varied in the range of  $(2-9) \times 10^6 \text{ cm}^{-3}$  and  
240  $(2-14) \times 10^8 \text{ cm}^{-3}$ , respectively. As in previous campaigns, the largest OH concentrations appeared around noontime and  
241 showed a high correlation with  $j(\text{O}^1\text{D})$ , a proxy for the solar UV radiation driving much of the primary radical production (Tan  
242 et al., 2019).

243 Figure 3 (a-b) shows the diurnal profiles of the observed and modeled HOx concentrations. The HOx radicals showed similar  
244 diurnal behavior to those reported in other campaigns (Ma et al., 2019a; Tan et al., 2017; Tan et al., 2019; Tan et al., 2018; Yang  
245 et al., 2021). The observed OH and HO<sub>2</sub>\* concentrations reached a maximum around 12:00 and 13:30, respectively. The  
246 diurnal maxima of the observed and modeled OH concentrations were  $4.5 \times 10^6 \text{ cm}^{-3}$  and  $3.5 \times 10^6 \text{ cm}^{-3}$ . Compared to the  
247 other campaigns conducted in PRD (Backgarden and Heshan), the diurnal maximum of the observed OH concentration in  
248 Shenzhen was equal to that observed in Heshan, but much lower than that observed in Backgarden where the observed OH  
249 concentration was nearly  $15 \times 10^6 \text{ cm}^{-3}$  (Hofzumahaus et al., 2009; Tan et al., 2019). The higher OH concentration at  
250 Backgarden site was closely correlated to the stronger solar radiation, as shown in Table S3 in the Supplementary Information.  
251 The diurnal observed and modeled OH concentrations agreed within their  $1-\sigma$  uncertainties of measurement and simulation  
252 (11% and 40%). However, when the NO mixing ratio (Fig. 2) dropped from 10:00 gradually, a systematic difference existed,  
253 with the observed OH concentration being about  $1 \times 10^6 \text{ cm}^{-3}$  higher than the modeled OH concentration. The OH  
254 concentrations observed in the environments with low NO levels were underestimated by the state-of-the-art models at  
255 Backgarden (summer) and Heshan (autumn) sites in PRD as well, and the OH underestimation was identified to be universal  
256 at low NO conditions in China (Lu et al., 2013; Lu et al., 2012; Ma et al., 2019a; Tan et al., 2017; Yang et al., 2021; Ma et al.,  
257 2022b). The reason on OH underestimation was further discussed in Section 4.1.

258



259  
 260 **Figure 3: (a-b) The diurnal profiles of the observed and modeled OH,  $\text{HO}_2^*$  and  $\text{HO}_2$  concentrations. (c) The diurnal profiles of the**  
 261 **modeled  $k_{\text{OH}}$ . (d) The composition of the modeled  $k_{\text{OH}}$ . The red areas in (a-b) denote  $1-\sigma$  uncertainties of the observed OH and  $\text{HO}_2^*$**   
 262 **concentrations. The blue areas in (a-b) denote  $1-\sigma$  uncertainties of the modeled OH and  $\text{HO}_2^*$  concentrations, and the dark grey**  
 263 **area in (b) denotes  $1-\sigma$  uncertainties of the modeled  $\text{HO}_2$  concentrations. The grey areas in (a-c) denote nighttime. ACD denotes**  
 264 **acetaldehydes. ALD denotes the C3 and higher aldehydes. ACT and KET denote acetone and ketones. MACR and MVK denote**  
 265 **methacrolein and methyl vinyl ketone.**

266 The diurnal maximum of the observed  $\text{HO}_2^*$ , the modeled  $\text{HO}_2^*$  and the modeled  $\text{HO}_2$  concentrations were  $4.2 \times 10^8 \text{ cm}^{-3}$ ,  
 267  $6.1 \times 10^8 \text{ cm}^{-3}$ , and  $4.4 \times 10^8 \text{ cm}^{-3}$ , respectively. The difference between the modeled  $\text{HO}_2^*$  and  $\text{HO}_2$  concentrations can be  
 268 considered a modeled  $\text{HO}_2$  interference from  $\text{RO}_2$  (Lu et al., 2012). The  $\text{RO}_2$  interference was small in the morning, while it  
 269 became larger in the afternoon. It ranged within 23%-28% during the daytime (08:00-17:00), which was comparable with  
 270 those at the Backgarden and Yufa sites in China, Borneo rainforest in Malaysia (OP3 campaign, aircraft), and UK (RONOCO  
 271 campaign, aircraft) (Lu et al., 2012; Lu et al., 2013; Jones et al., 2011; Stone et al., 2014). The observed  $\text{HO}_2^*$  was overestimated  
 272 by the model, indicating the  $\text{HO}_2$  heterogeneous uptake might have a significant impact during this campaign. The diurnal  
 273 maximum of  $\text{HO}_2^*$  concentration observed in Shenzhen was much lower than those observed at the Yufa and Backgarden sites  
 274 (Hofzumahaus et al., 2009; Lu et al., 2012; Lu et al., 2013). The high modeled  $\text{HO}_2/\text{OH}$  ratio around noontime (11:00-15:00),  
 275 which was about 138, was found in this campaign, which was higher than those at the Backgarden and Chengdu sites (Yang  
 276 et al., 2021; Hofzumahaus et al., 2009). High  $\text{HO}_2/\text{OH}$  ratio is normally found only in clean air at low  $\text{NO}_x$  ( $= \text{NO} + \text{NO}_2$ )  
 277 concentrations (Hofzumahaus et al., 2009; Stevens et al., 1997). As an indicator that can reflect the interconversion reaction  
 278 between  $\text{HO}_2$  and OH, the conversion efficiency in this campaign was slightly slower than those at the Backgarden and  
 279 Chengdu sites.

### 280 3.3 OH reactivity

281  $k_{\text{OH}}$  is the pseudo-first-order loss rate coefficient of OH radicals, and it is equivalent to the reciprocal OH lifetime (Fuchs et

282 al., 2017; Lou et al., 2010; Yang et al., 2019). In this campaign,  $k_{\text{OH}}$  was measured only for several days (05-19 October 2018)  
283 by the LIP-LIF system, which has been reported in the previous study (Liu et al., 2019). The timeseries of the observed and  
284 modeled  $k_{\text{OH}}$  during 05-19 October 2018 are presented in Fig. S3 in the Supplementary Information. A good agreement between  
285 the observed  $k_{\text{OH}}$  and modeled  $k_{\text{OH}}$  within the uncertainties was achieved, and thus the model can be believed to reproduce the  
286 observed  $k_{\text{OH}}$  values within the whole campaign. Moreover, to reflect the  $k_{\text{OH}}$  in the whole campaign, the modeled values were  
287 shown in the  $k_{\text{OH}}$  diurnal profiles (Fig. 3 (c)) and  $k_{\text{OH}}$  timeseries (Fig. S2 (c)) during 05-28 October 2018. The modeled  $k_{\text{OH}}$   
288 showed a weak diurnal variation and varied from  $18 \text{ s}^{-1}$  to  $22 \text{ s}^{-1}$ . Compared to the  $k_{\text{OH}}$  variation in Shenzhen, the  $k_{\text{OH}}$  observed  
289 at the Backgarden and Heshan sites in PRD showed a stronger diurnal variation, with a minimum value at around noontime  
290 and a maximum value at daybreak. Additionally, the  $k_{\text{OH}}$  values in this campaign were lower than those at Backgarden ( $20\text{-}50$   
291  $\text{s}^{-1}$ ) and Heshan ( $22\text{-}32 \text{ s}^{-1}$ ) sites (Lou et al., 2010; Tan et al., 2019). Similar with the good agreement between the observed and  
292 modeled  $k_{\text{OH}}$  during the several days in Shenzhen, the observed  $k_{\text{OH}}$  in Backgarden was matched well with the modeled  $k_{\text{OH}}$   
293 which has included the OVOCs reactivity. In terms of the  $k_{\text{OH}}$  in Heshan, Tan et al. (2019) reported that only half of the  
294 observed  $k_{\text{OH}}$  was explained by the calculated  $k_{\text{OH}}$  which was calculated from the measured trace gas concentrations. The  
295 missing  $k_{\text{OH}}$  in Heshan was likely caused by unmeasured VOCs, demonstrating the necessary to measure more abundant VOCs  
296 species, especially OVOCs species.

297 As shown in Fig. 3 (d), we presented the composition of modeled  $k_{\text{OH}}$ . The inorganic compounds contributed approximately  
298 31% to  $k_{\text{OH}}$ , in which the CO and NO<sub>x</sub> reactivity accounted for 10% and 21%, respectively. The NO<sub>x</sub> reactivity was displayed  
299 versus time, with a maximum during the morning peak. The peak concentration during the morning peak was associated with  
300 traffic emissions.

301 Compared with the inorganic reactivity, the larger fraction of  $k_{\text{OH}}$  came from the VOCs group, with a contribution of 69%  
302 to  $k_{\text{OH}}$ . The contribution of alkanes, alkenes, and aromatics were 15%, 10%, and 12%, respectively. The isoprene reactivity  
303 related to temperature was mainly concentrated during the daytime, whereas the aromatics reactivity at night was higher. As  
304 for the OVOCs species, we measured several OVOCs species, including HCHO, acetaldehydes (ACD) and higher aldehydes  
305 (ALD), acetone (ACT), ketones (KET) and isoprene oxidation products (methacrolein (MACR) and methyl vinyl ketone  
306 (MVK)), and thus we constrained these species in the model. The constrained OVOCs species accounted for 18% in the total  
307  $k_{\text{OH}}$ , where HCHO, ACD, and ALD were the major contributors, with contributions of 18%, 32%, and 38% to the constrained  
308 OVOCs, respectively. The contribution of aldehydes in this study (16%) was larger than that in Beijing (Whalley et al., 2021)  
309 and smaller with that in Wangdu (Fuchs et al., 2017). The remaining reactivity was attributed to the unconstrained OVOCs  
310 reactivity, which came from the model-generated intermediate species (glyoxal, methylglyoxal, methyl ethyl ketone, methanol,  
311 etc.), with a contribution of 11% to the total  $k_{\text{OH}}$ . Large fraction of OVOCs reactivities in  $k_{\text{OH}}$  was also found in some previous  
312 studies (Lou et al., 2010; Lu et al., 2013; Fuchs et al., 2017; Whalley et al., 2021). About 50% of  $k_{\text{OH}}$  was explained by OVOCs  
313 at Backgarden site, and HCHO, ACD and ALD, and oxygenated isoprene products were the most important OH reactants in

314 OVOCs, with a contribution of 30-40%, and other 10-20% came from other oxygenated compounds (ketones, dicarbonyl  
315 compounds, alcohols, hydroperoxides, nitrates etc.) (Lou et al., 2010). HCHO, ACD, MVK, MVCR and glyoxal accounted for  
316 one-third of the total  $k_{OH}$  at Wangdu site (Fuchs et al., 2017). The large unconstrained OVOCs reactivity indicated it is  
317 necessary to measure more VOCs species in the future.

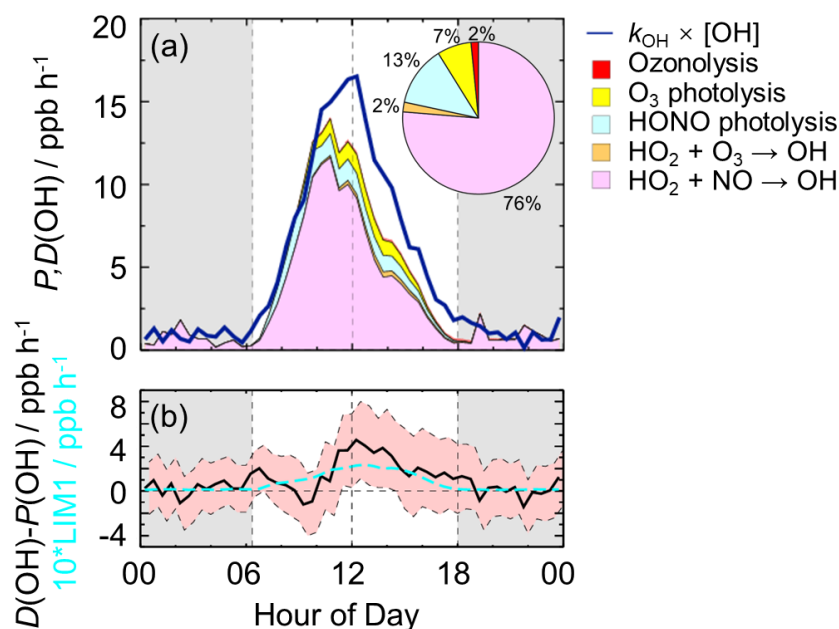
## 318 4. Discussion

### 319 4.1 Radical closure experiment

320 In this study, we conducted OH radical closure experiment which is called OH experimental budget as well. As discussed in  
321 Section 3.3, it is believed that the model can reproduce the observed  $k_{OH}$ . Herein, to conduct the OH experiment budget in the  
322 whole campaign, we used the modeled  $k_{OH}$  to calculate the OH destruction rate because the  $k_{OH}$  was only measured on several  
323 days. The diurnal profiles of OH production and destruction rates, and the compositions of OH production rate were displayed  
324 in Fig. 4, with maxima of 14 ppb h<sup>-1</sup> and 17 ppb h<sup>-1</sup> around noontime, respectively. The OH production rate from known sources  
325 is quantified from the primary sources (photolysis of HONO, photolysis of O<sub>3</sub>, ozonolysis of alkenes) and secondary sources  
326 (dominated by HO<sub>2</sub> + NO, and HO<sub>2</sub> + O<sub>3</sub>). The primary and secondary sources accounted for 78% and 22% of the total  
327 calculated production rate, respectively. Similar with the prior studies, the largest fraction of OH production rate came from  
328 HO<sub>2</sub> + NO, with a contribution up to 76% of the known OH production rate. As the major primary OH sources, the HONO  
329 and O<sub>3</sub> photolysis contributed 13% and 7% to the total calculated OH production rate, respectively.

330 The OH production rate matched well with the destruction rate only in the early morning to about 10:00. Thereafter, the OH  
331 destruction rate was larger than the production rate, which could explain the underestimation of OH concentration by the model.  
332 As shown in Fig. 4 (b), the discrepancy between the OH production and destruction rates at around 11:00-15:00, which was  
333 approximately of (3.1~4.6) ppb h<sup>-1</sup>, cannot be explained by the combined experimental uncertainties. The discrepancy was  
334 attributed to the missing OH sources because  $k_{OH}$  was constrained in this study. The biggest additional OH source was  
335 approximately 4.6 ppb h<sup>-1</sup>, which occurred at about 12:00, when the OH production and destruction rates were 11.9 ppb h<sup>-1</sup>  
336 and 16.5 ppb h<sup>-1</sup>, respectively. The unknown OH source accounted for about one third of the total OH production rate,  
337 indicating the exploration of missing OH source was significant to study the radical chemistry. It is noted that the OH  
338 production rate was overestimated because we used HO<sub>2</sub>\* concentrations instead of HO<sub>2</sub> concentrations here. Thus, the  
339 missing OH source was the lower limit here, demonstrating more unknown OH sources need to be further explored. Details  
340 on unknown OH sources are given below (Sect. 4.2).

341



342

343 **Figure 4: (a) The diurnal profiles of OH production and destruction rates and the proportions of different known sources in the**  
 344 **calculated production rate during the daytime. The blue line denotes the OH destruction rate, and the colored areas denote the**  
 345 **calculated OH production rates from the known sources. (b) The missing OH source which was the discrepancy between the OH**  
 346 **destruction and production rates, and the OH production rate which was ten times the production rate derived from LIM1**  
 347 **mechanism. The red shaded areas denote the combined uncertainty from the experimental errors of the measured quantities (Table**  
 348 **S1) and the reaction rate coefficients. The grey areas denote nighttime.**

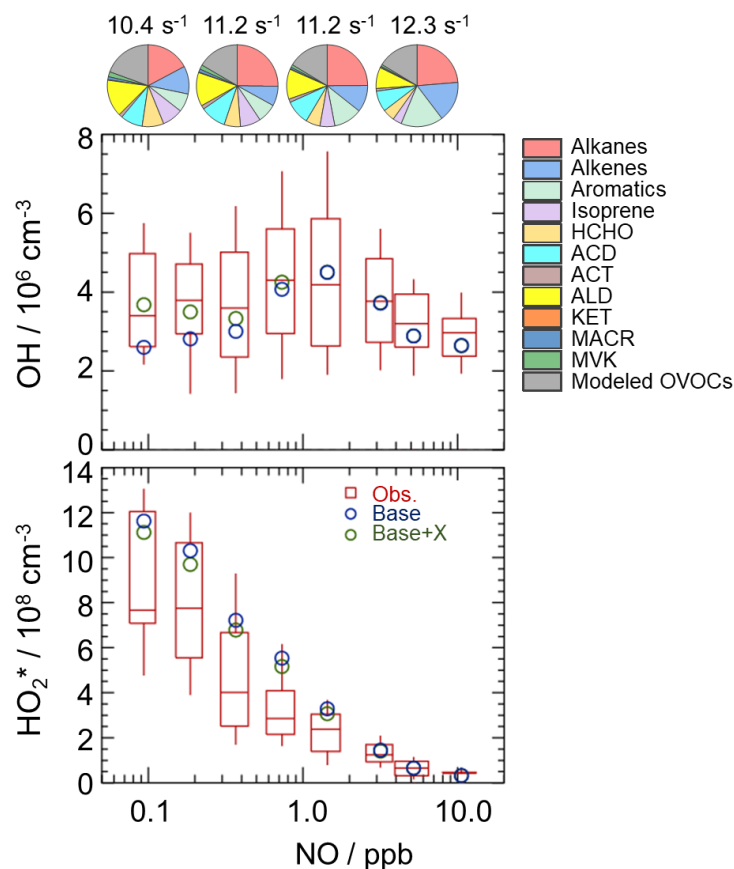
349

## 350 4.2 Radical chemistry in low NO regime

### 351 4.2.1 Influencing factors of OH underestimation

352 As analyzed in Sect. 4.1, the underestimation of OH concentration was attributable to the missing OH source. It is necessary  
 353 to explore the influencing factor for gaining further insight into the missing source. Scientists reported that more significant  
 354 OH underestimation would appear with the decreasing NO concentration and increasing isoprene concentration (Lu et al.,  
 355 2012;Ren et al., 2008;Hofzumahaus et al., 2009;Lelieveld et al., 2008;Whalley et al., 2011;Tan et al., 2017;Yang et al., 2021).  
 356 Herein, we further explored the effect of NO concentration on missing OH source. The NO dependence on observed and  
 357 modeled HOx concentrations and the NO dependence on HOx observed-to-modeled ratios were illustrated in Fig. 5 and Fig.  
 358 S4. The OH concentrations were normalized by the averaged  $j(\text{O}^1\text{D})$  to eliminate the influence of radiation on radicals. The  
 359 OH concentration showed an increasing trend with the increase of NO concentrations in low NO regime (below 1 ppb) due to  
 360 the increased OH radicals from propagation via peroxy reactions with NO, and then decreased with the increase of NO  
 361 concentrations in high NO regime (above 1 ppb) due to the OH loss by the reactions via  $\text{NO}_2$  (Ehhalt, 1999). The base model  
 362 can reproduce the observed OH concentration in high NO regime, while underestimate OH concentration in low NO regime.  
 363 As for  $\text{HO}_2^*$  radicals, the observed and modeled  $\text{HO}_2^*$  concentrations decreased with the increase of NO concentrations. The

364 model overestimated the observations, indicating that the heterogeneous uptake might make a significant role in HO<sub>2</sub> sinks in  
 365 this campaign. Overall, NO<sub>x</sub> plays a crucial role in radical chemistry due to their impact on radical propagation and termination  
 366 reactions.



367  
 368 **Figure 5: NO dependence on OH and HO<sub>2</sub>\* radicals. The red box-whisker plots give the 10%, 25%, median, 75%, and 90% of the**  
 369 **HO<sub>x</sub> observations. The blue circles show the median values of the HO<sub>x</sub> simulations by the base model, and the green circles show**  
 370 **the HO<sub>x</sub> simulations by the model with X mechanism. Total VOCs reactivity and their organic speciation are presented by pie charts**  
 371 **at the different NO intervals at the top. Only daytime values and NO concentration above the detection limit of the instrument were**  
 372 **chosen. ACD and ACT denote acetaldehyde and acetone, respectively. ALD denotes the C3 and higher aldehydes. KET denotes**  
 373 **ketones. MACR and MVK, which are both the isoprene oxidation products, denote methacrolein and methyl vinyl ketone,**  
 374 **respectively.**

375 To further explore the influencing factors of OH underestimation, we presented the speciation VOCs reactivity under the  
 376 different NO intervals, as shown in Fig. 5 and Table S4 in the Supplementary Information. The isoprene reactivity and total  
 377 OVOCs reactivity (the sum of HCHO, ACD, ACT, ALD, KET, MACR, MVK and the modeled OVOCs) increased with the  
 378 decrease of NO concentrations, while the anthropogenic VOCs reactivity (alkanes, alkenes and aromatics) was higher in high  
 379 NO regime. Additionally, the O<sub>3</sub> concentration in low NO regime was significantly higher than those in high NO regime, and  
 380 the temperature was slightly higher in low NO regime, demonstrating the photochemistry was more active in low NO regime  
 381 in this campaign. Overall, the photochemistry and composition of VOCs reactivity, especially the isoprene and OVOCs species  
 382 (mainly HCHO, ACD, ALD and the modeled OVOCs), might closely impact the missing OH sources.

## 383 4.2.2 Quantification of missing OH sources

384 Hofzumahaus et al. (2009) proposed an existence of a pathway for the regeneration of OH independent of NO, including the  
385 conversions of  $\text{RO}_2 \rightarrow \text{HO}_2$  and  $\text{HO}_2 \rightarrow \text{OH}$  by a numerical species called X. With a retrospective analysis, the unclassical  
386 OH recycling pathway was identified to be universal at low NO conditions in China. The amount of X varies with  
387 environmental conditions, and the X concentrations were 0.85 ppb, 0.4 ppb, 0.1 ppb, 0.4 ppb, 0.1 and 0.25 ppb at Backgarden,  
388 Yufa, Wangdu, Heshan, Taizhou, and Chengdu sites (Hofzumahaus et al., 2009; Lu et al., 2012; Lu et al., 2013; Tan et al.,  
389 2017; Yang et al., 2021; Ma et al., 2022b).

390 In this study, we tested this unclassical X mechanism. Good agreement between observations and simulations of OH radicals  
391 was achieved when a constant mixing ratio of 0.1 ppb of X was added into the base model. As shown in Fig. 5, the model with  
392 X mechanism agreed with the observed OH concentrations even at low NO conditions. Unclassical OH recycling was identified  
393 again in this study. Nevertheless, X is an artificial species that behaves like NO, and thus the nature of X is still unknown to  
394 us. Compared to the Shenzhen site, the required X concentration at the Backgarden and Heshan sites in PRD was higher, which  
395 might be affected by the different air masses in the three sites. The  $k_{\text{OH}}$  at Shenzhen site was much lower than those at the  
396 Backgarden and Heshan sites (Lu et al., 2013), and a weaker diurnal variation of  $k_{\text{OH}}$  in Shenzhen was observed. Under the  
397 influence of the East Asian monsoon, the prevailing wind for PRD area is mostly southerly during the summer months and  
398 mostly northerly during the winter months (Fan et al., 2005; Zhang et al., 2008). The Backgarden site is located in Guangzhou,  
399 and the Heshan site is located in Jiangmen. The two cities are along the north-south axis, and thus the air masses of the  
400 Backgarden and Heshan sites are intimately linked with each other, while the air mass in Shenzhen is more similar to Hongkong  
401 (Zhang et al., 2008). Compared to the VOCs reactivity in the air mass at Backgarden and Yufa sites reported by Lu et al. (2013),  
402 lower isoprene reactivity and OVOCs reactivity were observed in Shenzhen site. As discussed in Section 4.2.1, the OH  
403 underestimation might be closely related to the composition of VOCs reactivity. Therefore, further exploration of this  
404 unclassical OH recycling is needed to improve our understanding of radical chemistry, especially the mechanisms related to  
405 isoprene and OVOCs.

406 As for the potential influence of isoprene and OVOCs on the missing OH source,  $\text{RO}_2$  isomerization reactions have also  
407 been shown to be of importance for the atmospheric fate of  $\text{RO}_2$  from isoprene (Peeters et al., 2009; Peeters et al., 2014). The  
408 latest isoprene isomerization mechanism, which is called LIM1, has been coupled into our current base model. However, LIM1  
409 mechanism was not included in the OH experimental budget which was conducted with the observations constrained, as shown  
410 in Section 4.1. Herein, we evaluated the contribution of LIM1 mechanism to the missing OH sources, as shown in Fig. 4 (b).  
411 LIM1 mechanism can explain approximately 7% of the missing OH sources during 10:00-16:00, when the missing OH  
412 production rate and the OH production rate derived from LIM1 mechanism were  $2.47 \text{ ppb h}^{-1}$  and  $0.17 \text{ ppb h}^{-1}$ , respectively.

413 Additionally, prior studies also reported that OH regeneration might be achieved from the oxidation of MACR and MVK,



414 which are the major first-generated products of isoprene (Fuchs et al., 2018;Fuchs et al., 2014). As a potential explanation for  
 415 the high OH concentration, the impacts of MACR and MVK oxidation were evaluated here. The modification of MACR  
 416 oxidation scheme added the H-migration reactions of MACR oxidation products (Fuchs et al., 2014). The modification of  
 417 MVK oxidation scheme added the reactions of MVK oxidation products with HO<sub>2</sub> radicals and the H-migration reactions of  
 418 MVK oxidation products (Fuchs et al., 2018). As presented in Fig. S5 in the Supplementary Information, no significant of the  
 419 MACR and MVK oxidation schemes was found in this campaign.

420 Overall, a large part of missing OH sources was not explained by the isoprene chemistry. In the future, the impact of OVOCs  
 421 species which was another potential OH source on missing OH sources need to be further evaluated.

### 422 4.3 HO<sub>2</sub> heterogeneous uptake

423 The HO<sub>2</sub><sup>\*</sup> overestimation was identified by comparing the observed and modeled HO<sub>2</sub><sup>\*</sup> concentrations in Sect. 3.2 and Sect.  
 424 4.2.1. The HO<sub>2</sub> heterogeneous uptake has been proposed to be a potential sink of HO<sub>2</sub> radicals, and thus could influence the  
 425 radical chemistry and the formation of secondary pollution, especially in high-aerosol environments (Song et al., 2021;Song  
 426 et al., 2022;Tan et al., 2020;Kanaya et al., 2000;Kanaya et al., 2007;Li et al., 2019). The impact of HO<sub>2</sub> uptake chemistry on  
 427 radical concentration is different under different environmental conditions (Whalley et al., 2015;Mao et al., 2010;Li et al.,  
 428 2019). To evaluate the contribution of HO<sub>2</sub> uptake chemistry to radical concentrations in this study, we coupled HO<sub>2</sub>  
 429 heterogeneous uptake into the base model (RACM2-LIM1) and conducted three sensitivity experiments, as shown in R1 and  
 430 Eq. (3).



$$432 k_{\text{HO}_2+\text{aerosol}} = \frac{\gamma \cdot \text{ASA} \cdot v_{\text{HO}_2}}{4} \quad (3)$$

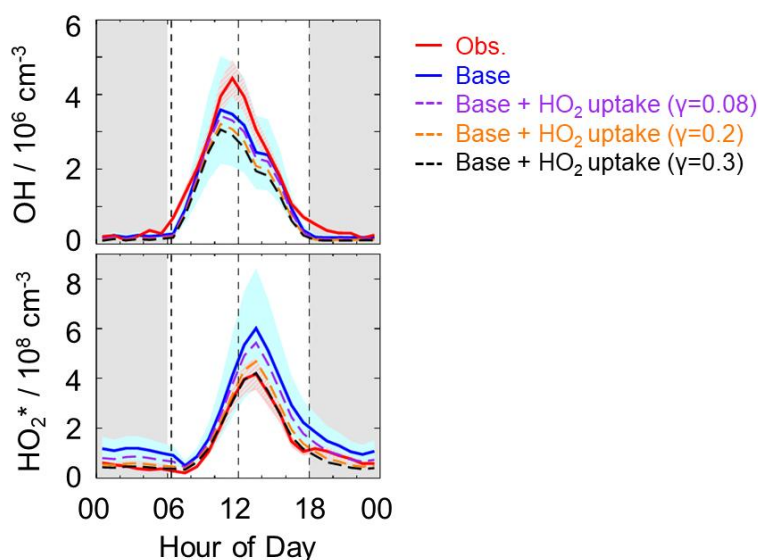
433 where ASA [μm<sup>2</sup> cm<sup>-3</sup>], which represents the aerosol surface area concentration, can be estimated by multiplying the mass  
 434 concentration of PM<sub>2.5</sub> [μg m<sup>-3</sup>] by 20 here because there were no direct ASA observations in this campaign (Chen et al.,  
 435 2019;Wang et al., 2017b).  $v_{\text{HO}_2}$ , which can be calculated by Eq. (4), refers to the mean molecular velocity of HO<sub>2</sub> with a unit  
 436 of cm s<sup>-1</sup>.

$$437 v_{\text{HO}_2} = \sqrt{\frac{8 \cdot R \cdot T}{0.033 \cdot \pi}} \quad (4)$$

438 where T [K] and R [J mol<sup>-1</sup> K<sup>-1</sup>] denote the ambient temperature and gas constant.  $\gamma$ , the HO<sub>2</sub> effective uptake coefficient,  
 439 parameterizes the influence of some processes (Tan et al., 2020).  $\gamma$  varies in the highly uncertain range of 0-1 (Song et al.,  
 440 2022), and is the most critical parameter to impact HO<sub>2</sub> uptake chemistry. Only several observations of  $\gamma$  have been reported  
 441 (Taketani et al., 2012;Zhou et al., 2021;Zhou et al., 2020). The measured  $\gamma$  at the Mt. Tai site and Mt. Mang site were 0.13-  
 442 0.34 and 0.09-0.40, respectively (Taketani et al., 2012). The average value of the measured  $\gamma$  was 0.24 in Kyoto, Japan in the

443 summer of 2018 (Zhou et al., 2020). Zhou et al. (2021) reported the lower-limit values for median and average values of the  
 444 measured  $\gamma$  were 0.19 and  $0.23 \pm 0.21$  in Yokohama, Japan in the summer of 2019. Additionally, Li et al. (2018) set 0.2 as the  
 445 value of  $\gamma$  in the model, and Tan et al. (2020) calculated the  $\gamma$  of  $0.08 \pm 0.13$  by the analysis of the measured radical budget in  
 446 Wangdu.

447 Here, we applied the two  $\gamma$  (0.2 and 0.08), which have been used in the model, to evaluate the impact of  $\text{HO}_2$  uptake on  
 448 radical concentrations, as shown in Fig. 6. The modeled  $\text{HO}_2^*$  cannot match well with the observations when  $\gamma$  of 0.08 and 0.2  
 449 was set in the model. As the  $\gamma$  increased to approximately 0.3, good agreement between the modeled and observed  $\text{HO}_2^*$   
 450 concentration was achieved, demonstrating that a significant heterogeneous uptake might exist in this campaign. It should be  
 451 noted that the  $\text{HO}_2$  heterogeneous uptake ( $\gamma = 0.3$ ) reduced the modeled OH concentrations by around 20% compared to the  
 452 OH simulations in the base model during the daytime (08:00-18:00). Sensitivity tests illustrated that good agreements of OH  
 453 observations-simulations and  $\text{HO}_2^*$  observations-simulations were both achieved when the amount of X changed from 0.1 ppb  
 454 to 0.25 ppb and the  $\text{HO}_2$  effective uptake coefficient was 0.3, as shown in Fig. S6 in the Supplementary Information. Compared  
 455 to the Backgarden and Heshan sites, the amount of X in Shenzhen was still lower despite a significant  $\text{HO}_2$  heterogeneous  
 456 uptake, which might be closely related to the environmental conditions as discussed in Sect. 4.2.

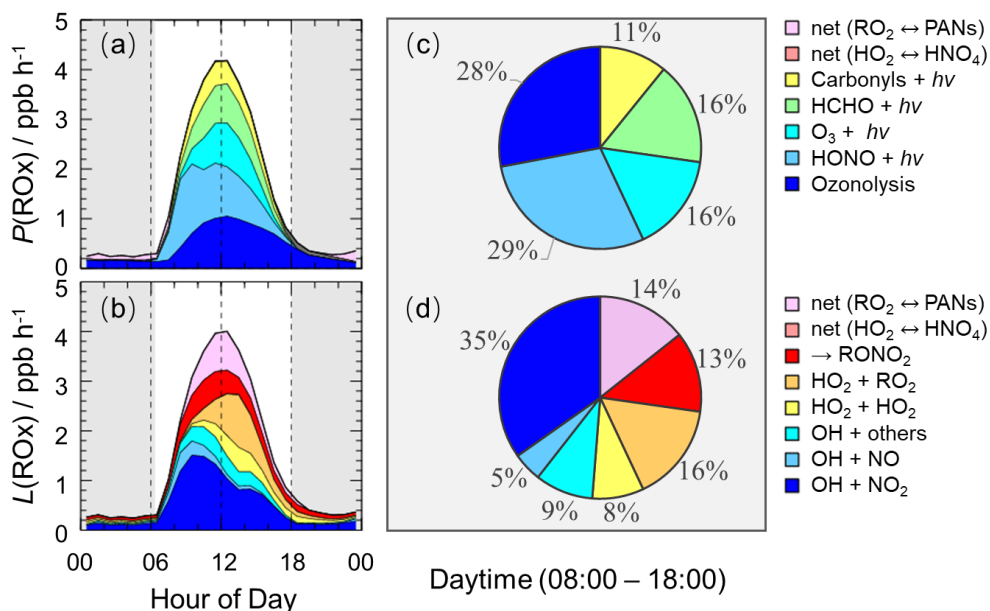


457  
 458 **Figure 6: The diurnal profiles of the observed and modeled radical concentrations. The red and blue areas denote 1- $\sigma$  uncertainties**  
 459 **of measured and simulated radical concentrations by the base model, respectively. The orange, purple and black lines denote the**  
 460 **simulations by the model which added the  $\text{HO}_2$  heterogeneous uptake with different uptake coefficient. The grey areas denote**  
 461 **nighttime.**

462 It is noted that the estimated strong influence is speculative because of the uncertainties of measurements and simulations.  
 463 Overall, the  $\gamma$  evaluated in this study was comparable with those observed at the Mt. Tai and Mt. Mang in China, and Kyoto  
 464 and Yokohama in Japan.

465 **4.4 Sources and sinks of ROx**

466 The detailed analysis of radical sources and sinks was crucial to exploring radical chemistry. The experimental budget for HO<sub>2</sub>  
 467 and RO<sub>2</sub> radicals could not be conducted because RO<sub>2</sub> was not measured during this campaign. Herein, we showed the  
 468 simulated results by the base model. Figure 7 illustrates the diurnal profiles of ROx primary production rate ( $P(\text{ROx})$ ) and  
 469 termination rate ( $L(\text{ROx})$ ), and the contributions of different channels during the daytime.



470  
 471 **Figure 7: The diurnal profiles of ROx primary production rate (a) and termination rate (b) simulated by the base model, and the**  
 472 **contributions of different channels to ROx primary production rate (c) and termination rate (d) during the daytime (08:00-18:00).**  
 473 **The grey areas denote nighttime.**

474 The ROx primary production and termination rates were basically in balance for the entire day, with maxima of 4 ppb h<sup>-1</sup>  
 475 around noontime. The ROx primary production rate was similar to those at Heshan (4 ppb h<sup>-1</sup>) and Wangdu (5 ppb h<sup>-1</sup>) sites,  
 476 but lower than those at Backgarden (11 ppb h<sup>-1</sup>), Yufa (7 ppb h<sup>-1</sup>), Taizhou (7 ppb h<sup>-1</sup>) and Chengdu (7 ppb h<sup>-1</sup>) sites (Lu et al.,  
 477 2013;Lu et al., 2012;Tan et al., 2017;Tan et al., 2019;Yang et al., 2021). During the daytime, the  $P(\text{ROx})$  mainly came from  
 478 the OH and HO<sub>2</sub> primary production. HONO and O<sub>3</sub> photolysis dominated the OH primary production, and HCHO photolysis  
 479 dominated the HO<sub>2</sub> primary production. Thus,  $P(\text{ROx})$  was dominated by the photolysis reactions, in which the photolysis of  
 480 HONO, O<sub>3</sub>, HCHO, and carbonyls accounted for 29%, 16%, 16%, and 11% during the daytime, respectively. In the early  
 481 morning, HONO photolysis was the most important primary source of ROx, and the contribution of O<sub>3</sub> photolysis became  
 482 progressively larger and was largest at noontime. A large discrepancy between the ratio of HONO photolysis rate to O<sub>3</sub>  
 483 photolysis rate in summer/autumn and that in winter occurs generally. The vast majority of OH photolysis source is attributed  
 484 to HONO photolysis in winter because of the higher HONO concentration and lower O<sub>3</sub> concentration. About half of  $L(\text{ROx})$   
 485 came from OH termination, which occurred mainly in the morning, and thereafter, radical self-combination gradually became  
 486 the major sink of ROx in the afternoon. OH + NO<sub>2</sub>, OH + NO, and OH + others contributed 35%, 5%, and 9% to  $L(\text{ROx})$ ,

487 respectively. HO<sub>2</sub> + HO<sub>2</sub> and HO<sub>2</sub> + RO<sub>2</sub> accounted for 8% and 16% in *L*(RO<sub>x</sub>).

#### 488 4.5 AOC evaluation

489 AOC controls the abundance of precursors and the production of secondary pollutants (Yang et al., 2020a; Elshorbany et al.,  
490 2009), and thus it is necessary to quantify AOC for understanding photochemical pollution. The AOC has been evaluated in  
491 previous studies, as shown in Table 1. Overall, the AOC values in summer are higher than those in autumn and winter, and the  
492 values at lower latitudes are higher than those at higher latitudes for the same season. The vast majority of AOC in previous  
493 studies are evaluated based on the non-observed radical concentrations.

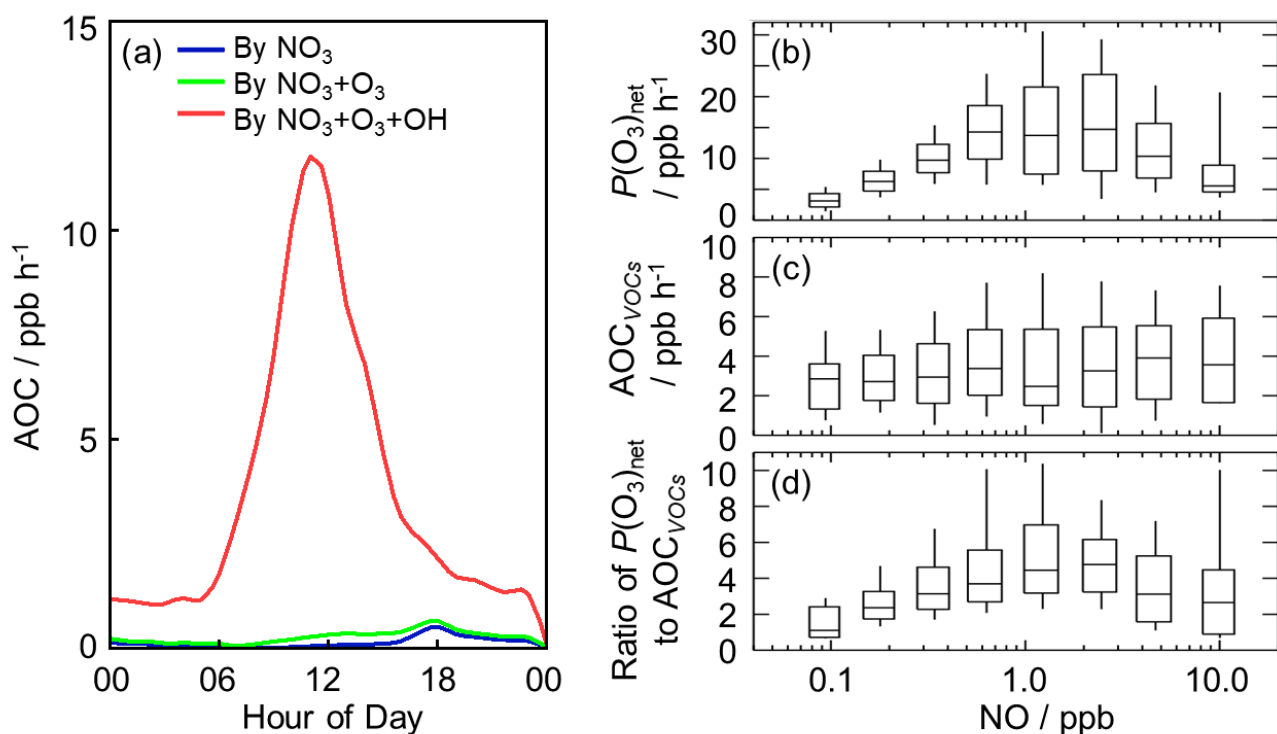
494 **Table 1: Summary of OH concentrations and AOC values reported in previous field campaigns.**

Location	Season, year	Site	Observed or non-observed radicals	of OH	AOC / 10 <sup>8</sup> molecules cm <sup>-3</sup> s <sup>-1</sup>	References
Beijing, China	summer, 2018	urban	non-observed values		0.89 <sup>a</sup>	(Liu et al., 2021)
Beijing, China	summer, 2018	suburban	non-observed values		0.85 <sup>a</sup>	(Liu et al., 2021)
Beijing, China	winter, 2018	urban	non-observed values		0.21 <sup>a</sup>	(Liu et al., 2021)
Beijing, China	winter, 2018	suburban	non-observed values		0.16 <sup>a</sup>	(Liu et al., 2021)
Hongkong, China	summer, 2011	suburban	non-observed values		2.04 <sup>a,b</sup>	(Xue et al., 2016)
Santiago, Chile	summer, 2005	urban	non-observed values		3.4 <sup>a</sup>	(Elshorbany et al., 2009)
Hong Kong, China	late summer, 2012	coastal	non-observed values		1.4 <sup>c</sup>	(Li et al., 2018)
Hong Kong, China	autumn, 2012	coastal	non-observed values		0.62 <sup>c</sup>	(Li et al., 2018)
Hong Kong, China	winter, 2012	coastal	non-observed values		0.41 <sup>c</sup>	(Li et al., 2018)
Shanghai, China	summer, 2018	urban	non-observed values		1.0 <sup>c</sup>	(Zhu et al., 2020)
Berlin, Germany	summer, 1998	suburban	non-observed values		0.14 <sup>d</sup>	(Geyer et al., 2001)
Xianghe, China	autumn, 2019	suburban	non-observed values		0.49 <sup>c</sup>	(Yang et al., 2020a)
Beijing, China	summer, 2014	urban	non-observed values		1.7 <sup>a</sup>	(Feng et al., 2021)

495 Note that:

496 <sup>a</sup> Peak values in the diurnal profiles; <sup>b</sup> Values on 25 August 2021; <sup>c</sup> Maximum over a period of time; <sup>d</sup> Maximum on some day.

497 Herein, we explored the AOC in Shenzhen based on the observed radical concentrations for the first time. As illustrated in  
498 Fig. 8 (a), the diurnal profile of AOC exhibited a unimodal pattern, which was the same as the diurnal profile of OH  
499 concentration and *j*(NO<sub>2</sub>), with a peak around noontime. The diurnal peak of AOC was 0.75 × 10<sup>8</sup> molecules cm<sup>-3</sup> s<sup>-1</sup> (11.8 ppb  
500 h<sup>-1</sup>). Comparatively, AOC in this study was comparable to those evaluated in Beijing (summer, 2018) and Hong Kong (autumn,  
501 2012) (Li et al., 2018; Liu et al., 2021), but much lower than those evaluated in Hong Kong (summer, 2011) and Santiago



503  
 504 **Figure 8: (a) The diurnal profiles of AOC in this campaign. (b) NO dependence on  $P(O_3)_{net}$  during the daytime. (c) NO dependence**  
 505 **on  $AOC_{VOCs}$  during the daytime, and  $AOC_{VOCs}$  denotes the atmospheric oxidation capacity only from the VOCs oxidation. (d) NO**  
 506 **dependence on the ratio of  $P(O_3)_{net}$  to  $AOC_{VOCs}$  during the daytime. The box-whisker plots in (b-d) give the 10%, 25%, median, 75%,**  
 507 **and 90%  $P(O_3)_{net}$ ,  $AOC_{VOCs}$  and the ratio of  $P(O_3)_{net}$  to  $AOC_{VOCs}$ , respectively.**

508 As expected, the dominant contributor to the AOC during this campaign was OH, followed by  $O_3$  and  $NO_3$ . Figure S7 shows  
 509 the fractional composition of the total AOC. The OH radical contributed about 95.7% of AOC during the daytime (08:00-  
 510 18:00).  $O_3$ , as the second important oxidant, accounted for only 2.9% of AOC during the daytime. The contribution of  $NO_3$  to  
 511 AOC during the daytime can be ignored, with a contribution of 1.4%. At night, the contributions of  $O_3$  and  $NO_3$  to AOC were  
 512 higher. OH,  $O_3$  and  $NO_3$  accounted for 75.6%, 6.4%, and 18% in the first half of night (18:00-24:00), and they accounted for  
 513 87.7%, 5%, and 7.3% in the second half of night (00:00-08:00).

514 As the indicator for secondary pollution, net  $O_3$  production rate,  $P(O_3)_{net}$ , can be calculated from the  $O_3$  formation rate ( $F(O_3)$ )  
 515 and the loss rate ( $L(O_3)$ ), as shown in Eq. (5-7) (Tan et al., 2017). The diurnal profiles of the speciation  $F(O_3)$  and  $L(O_3)$  were  
 516 shown in Fig. S8 in the Supplementary Information. The diurnal maxima of the modeled  $F(O_3)$  and  $L(O_3)$  were 18.9 ppb h<sup>-1</sup>  
 517 and 2.8 ppb h<sup>-1</sup>, with the maximum  $P(O_3)_{net}$  of 16.1 ppb h<sup>-1</sup> at around 11:00. The modeled  $P(O_3)_{net}$  in this study was comparable  
 518 to the net  $O_3$  production rate in Wangdu in summer (Tan et al., 2017), while the net ozone production rate in Shenzhen was  
 519 much higher than the gross  $O_3$  production rate in Beijing in winter (Tan et al., 2018).

$$520 F(O_3) = k_{HO_2+NO}[HO_2][NO] + \sum_i k_{RO_2i+NO}[RO_2]_i[NO] \quad (5)$$

$$521 L(O_3) = \theta j(O^1D)[O_3] + k_{O_3+OH}[O_3][OH] + k_{O_3+HO_2}[O_3][HO_2] + (\sum(k_{alkenes+O_3}^i[alkenes^i]))[O_3] \quad (6)$$

$$P(\text{O}_3)_{\text{net}} = F(\text{O}_3) - L(\text{O}_3) - k_{\text{NO}_2+\text{OH}}[\text{NO}_2][\text{OH}] \quad (7)$$

where  $\theta$  is the fraction of  $\text{O}^1\text{D}$  from ozone photolysis that reacts with water vapor.

Herein, we presented the NO dependence on  $P(\text{O}_3)_{\text{net}}$ ,  $\text{AOC}_{\text{VOCs}}$ , and the ratio of  $P(\text{O}_3)_{\text{net}}$  to  $\text{AOC}_{\text{VOCs}}$  in Fig. 8 (b-d), in which  $\text{AOC}_{\text{VOCs}}$  denotes the atmospheric oxidation capacity only from the VOCs oxidation, which includes the channels of primary VOCs (excluding OVOCs, and mainly alkanes, alkenes, aromatics and isoprene) with OH radicals. An upward trend of  $P(\text{O}_3)_{\text{net}}$  was presented with the increase of NO concentration when NO concentration was below 1 ppb, while  $P(\text{O}_3)_{\text{net}}$  decreased with the increase of NO concentration because  $\text{NO}_2$  became the sink of OH radicals gradually when NO concentration was above 1 ppb. In terms of the NO dependence on  $\text{AOC}_{\text{VOCs}}$ , no significant variation was found, indicating VOCs oxidation was weakly impacted by NO concentrations in this campaign. Since  $\text{AOC}_{\text{VOCs}}$  can represent the VOCs oxidant rate, and thus the ratio of  $P(\text{O}_3)_{\text{net}}$  to  $\text{AOC}_{\text{VOCs}}$  can reflect the yield of net ozone production from VOCs oxidation. Similar to  $P(\text{O}_3)_{\text{net}}$ , the ratios increased with the increase of NO concentration when NO concentration was below 1 ppb, while the ratios decreased with the increase of NO concentration when NO concentration was above 1 ppb, indicating the yield of net  $\text{O}_3$  production from VOCs oxidation would be lower within the low NO regime ( $< 1$  ppb) and high NO regime ( $> 1$  ppb). The median ratios ranged from 1.0 to 4.5, and the maximum of the median ratios existed when NO concentration was approximately 1 ppb, with a value of approximately 4.5. The nonlinear response of the yield of net ozone production to NO indicated that it is necessary to optimize the  $\text{NO}_x$  and VOC control strategies for the reduction of  $\text{O}_3$  pollution effectively.

## 5 Conclusions

The STORM field campaign was carried out at Shenzhen site in the autumn of 2018, providing the continuous OH and  $\text{HO}_2^*$  observations in PRD since the Heshan campaign in 2014. The maximum diurnal OH and  $\text{HO}_2^*$  concentrations, which were measured by the PKU-LIF system, were  $4.5 \times 10^6 \text{ cm}^{-3}$  and  $4.2 \times 10^8 \text{ cm}^{-3}$ , respectively. The observed OH concentration was equal to that measured at the Heshan site (autumn campaign) but was lower than those measured in the summer campaigns in China (Backgarden, Yufa, Wangdu, Taizhou and Chengdu sites). The observed  $\text{HO}_2^*$  concentrations included the true  $\text{HO}_2$  concentrations and an estimated interference from  $\text{RO}_2$  radicals, and was much lower than those measured at the Backgarden and Yufa sites in China.

The base model (RACM2-LIM1) could reproduce the observed OH concentration before 10:00, and thereafter, OH was underestimated by the model when NO concentration dropped to low levels. The results of the radical experimental budget indicated that OH underestimation was likely attributable to an unknown missing OH source at low NO regime. We diagnosed the missing OH source by sensitivity runs, and unclassical OH recycling was identified again in this study. Good agreement between the modeled and observed OH concentrations was achieved when a constant mixing ratio of the numerical species X,

552 equivalent to 0.1 ppb NO, was added into the base model. Additionally, we found isoprene and OVOCs might closely influence  
553 the missing OH sources by comparing the composition of VOCs reactivity under the different NO intervals. Isoprene  
554 isomerization mechanism (LIM1) can explain approximately 7% of the missing OH production rate, and no significant  
555 contribution of MACR and MVK oxidation was found. As another potential OH source, OVOCs species should be further  
556 explored to explain the remaining missing OH sources. As for HO<sub>2</sub> radicals, the overestimation of HO<sub>2</sub><sup>\*</sup> concentration was  
557 found, indicating that HO<sub>2</sub> heterogeneous uptake with the effective uptake coefficient of 0.3 might make a significant role in  
558 HO<sub>2</sub> sinks. Good agreements of OH observations-simulations and HO<sub>2</sub><sup>\*</sup> observations-simulations were both achieved when  
559 the amount of X changed from 0.1 ppb to 0.25 ppb and the HO<sub>2</sub> effective uptake coefficient was 0.3.

560 The quantification of production and destruction channels of ROx radicals is essential to explore the chemical processes of  
561 radicals. The ROx primary production and termination rates were balanced for the entire day, with maxima of 4 ppb h<sup>-1</sup>, similar  
562 to those at the Heshan and Wangdu sites. Photolysis channels dominated the ROx primary production rate, and the HONO, O<sub>3</sub>,  
563 HCHO, and carbonyls photolysis accounted for 29%, 16%, 16%, and 11% during the daytime, respectively. The most fraction  
564 of ROx termination rate came from the reaction of OH + NO<sub>2</sub> in the morning. The radical self-combination gradually became  
565 the major sink of ROx in the afternoon with the decreasing of NO concentrations. The reaction of OH + NO<sub>2</sub> and radical self-  
566 combination accounted for 35% and 24% during the daytime, respectively.

567 In this campaign, AOC exhibited well-defined diurnal patterns, with a peak of 11.8 ppb h<sup>-1</sup>. As expected, OH radicals, which  
568 were the dominant oxidant, accounted for 95.7% of the total AOC during the daytime. O<sub>3</sub> and NO<sub>3</sub> contributed 2.9% and 1.4%  
569 to total AOC during the daytime, respectively. The ratio of  $P(O_3)_{net}$  to AOC<sub>VOCs</sub>, which denotes the yield of net ozone production  
570 from VOCs oxidation, tended to increase and then decrease as NO concentration increased, with a range of 1.0-4.5. Optimizing  
571 the NOx and VOCs control strategies might be significant to realize the reduction of ozone concentrations based on the  
572 nonlinear relationship between the yield of net ozone production from VOCs oxidation and NO concentrations.

573  
574 **Data availability.** The data used in this study are available from the corresponding author upon request (k.lu@pku.edu.cn).

575  
576 **Author contributions.** YH Zhang and KD Lu conceived the study. XP Yang analyzed the data and wrote the manuscript with  
577 inputs from KD Lu. XP Yang, XF Ma, Y Gao contributed to the measurements of the HOx concentrations. All authors  
578 contributed to the discussed results and commented on the manuscript.

579  
580 **Competing interests.** The authors declare that they have no conflict of interest.

581  
582 **Acknowledgment.** The authors thank the science teams of the STORM-2018 campaign. This work was supported by the

583 Beijing Municipal Natural Science Foundation for Distinguished Young Scholars (JQ19031), the National Research Program  
584 for Key Issue in Air Pollution Control (2019YFC0214800), and the National Natural Science Foundation of China (Grants  
585 No. 91544225, 21522701, 91844301).

## 586 **Appendix A. Supplementary data**

### 587 **References**

- 588 Berndt, T., Chen, J., Kjaergaard, E. R., Moller, K. H., Tilgner, A., Hoffmann, E. H., Herrmann, H., Crounse, J. D., Wennberg,  
589 P. O., and Kjaergaard, H. G.: Hydrotrioxide (ROOOH) formation in the atmosphere, *Science*, 376, 979-+,  
590 10.1126/science.abn6012, 2022.
- 591 Brocco, D., Fratarcangeli, R., Lepore, L., Petricca, M., and Ventrone, I.: Determination of aromatic hydrocarbons in urban air  
592 of Rome, *Atmospheric Environment*, 31, 557-566, 10.1016/s1352-2310(96)00226-9, 1997.
- 593 Chen, X., Wang, H., Liu, Y., Su, R., Wang, H., Lou, S., and Lu, K.: Spatial characteristics of the nighttime oxidation capacity  
594 in the Yangtze River Delta, China, *Atmospheric Environment*, 208, 150-157, 10.1016/j.atmosenv.2019.04.012, 2019.
- 595 Ehhalt, D. H.: Photooxidation of trace gases in the troposphere, *Physical Chemistry Chemical Physics*, 1, 5401-5408,  
596 10.1039/a905097c, 1999.
- 597 Elshorbany, Y. F., Kurtenbach, R., Wiesen, P., Lissi, E., Rubio, M., Villena, G., Gramsch, E., Rickard, A. R., Pilling, M. J., and  
598 Kleffmann, J.: Oxidation capacity of the city air of Santiago, Chile, *Atmospheric Chemistry and Physics*, 9, 2257-2273,  
599 10.5194/acp-9-2257-2009, 2009.
- 600 Fan, S., Wang, A., Fan, Q., Liu, J., and Wang, B.: ATMOSPHERIC BOUNDARY LAYER CONCEPT MODEL OF THE  
601 PEARL RIVER DELTA AND ITS APPLICATION, *Journal of Tropical Meteorology*, 21, 286-292, 2005.
- 602 Feng, T., Zhao, S. Y., Hu, B., Bei, N. F., Zhang, X., Wu, J. R., Li, X., Liu, L., Wang, R. N., Tie, X. X., and Li, G. H.: Assessment  
603 of Atmospheric Oxidizing Capacity Over the Beijing-Tianjin-Hebei (BTH) Area, China, *Journal of Geophysical Research-*  
604 *Atmospheres*, 126, 18, 10.1029/2020jd033834, 2021.
- 605 Fittschen, C.: The reaction of peroxy radicals with OH radicals, *Chemical Physics Letters*, 725, 102-108,  
606 10.1016/j.cplett.2019.04.002, 2019.
- 607 Fittschen, C., Al Ajami, M., Batut, S., Ferracci, V., Archer-Nicholls, S., Archibald, A. T., and Schoemaeker, C.: ROOOH: a  
608 missing piece of the puzzle for OH measurements in low-NO environments?, *Atmospheric Chemistry and Physics*, 19, 349-  
609 362, 10.5194/acp-19-349-2019, 2019.
- 610 Fuchs, H., Holland, F., and Hofzumahaus, A.: Measurement of tropospheric RO<sub>2</sub> and HO<sub>2</sub> radicals by a laser-induced  
611 fluorescence instrument, *Review of Scientific Instruments*, 79, 10.1063/1.2968712, 2008.
- 612 Fuchs, H., Bohn, B., Hofzumahaus, A., Holland, F., Lu, K. D., Nehr, S., Rohrer, F., and Wahner, A.: Detection of HO<sub>2</sub> by laser-  
613 induced fluorescence: calibration and interferences from RO<sub>2</sub> radicals, *Atmospheric Measurement Techniques*, 4, 1209-1225,  
614 10.5194/amt-4-1209-2011, 2011.
- 615 Fuchs, H., Acir, I. H., Bohn, B., Brauers, T., Dorn, H. P., Häsel, R., Hofzumahaus, A., Holland, F., Kaminski, M., Li, X., Lu,  
616 K., Lutz, A., Nehr, S., Rohrer, F., Tillmann, R., Wegener, R., and Wahner, A.: OH regeneration from methacrolein oxidation  
617 investigated in the atmosphere simulation chamber SAPHIR, *Atmos. Chem. Phys.*, 14, 7895-7908, 10.5194/acp-14-7895-2014,  
618 2014.
- 619 Fuchs, H., Tan, Z., Hofzumahaus, A., Broch, S., Dorn, H.-P., Holland, F., Kuenstler, C., Gomm, S., Rohrer, F., Schrade, S.,  
620 Tillmann, R., and Wahner, A.: Investigation of potential interferences in the detection of atmospheric RO<sub>x</sub> radicals by laser-  
621 induced fluorescence under dark conditions, *Atmospheric Measurement Techniques*, 9, 1431-1447, 10.5194/amt-9-1431-2016,  
622 2016.
- 623 Fuchs, H., Tan, Z., Lu, K., Bohn, B., Broch, S., Brown, S. S., Dong, H., Gomm, S., Haeseler, R., He, L., Hofzumahaus, A.,  
624 Holland, F., Li, X., Liu, Y., Lu, S., Min, K.-E., Rohrer, F., Shao, M., Wang, B., Wang, M., Wu, Y., Zeng, L., Zhang, Y., Wahner,



625 A., and Zhang, Y.: OH reactivity at a rural site (Wangdu) in the North China Plain: contributions from OH reactants and  
626 experimental OH budget, *Atmospheric Chemistry and Physics*, 17, 645-661, 10.5194/acp-17-645-2017, 2017.

627 Fuchs, H., Albrecht, S., Acir, I.-H., Bohn, B., Breitenlechner, M., Dorn, H.-P., Gkatzelis, G. I., Hofzumahaus, A., Holland, F.,  
628 Kaminski, M., Keutsch, F. N., Novelli, A., Reimer, D., Rohrer, F., Tillmann, R., Vereecken, L., Wegener, R., Zaytsev, A.,  
629 Kiendler-Scharr, A., and Wahner, A.: Investigation of the oxidation of methyl vinyl ketone (MVK) by OH radicals in the  
630 atmospheric simulation chamber SAPHIR, *Atmospheric Chemistry and Physics*, 18, 8001-8016, 10.5194/acp-18-8001-2018,  
631 2018.

632 Gao, M., Li, H., Li, Y., Wei, J., Sun, Y., He, L., and Huang, X.: Source characteristics of water-soluble organic matters in  
633 PM<sub>2.5</sub> in the winter of Shenzhen, *China Environmental Science*, 38, 4017-4022, 2018.

634 Geyer, A., Alicke, B., Konrad, S., Schmitz, T., Stutz, J., and Platt, U.: Chemistry and oxidation capacity of the nitrate radical  
635 in the continental boundary layer near Berlin, *Journal of Geophysical Research-Atmospheres*, 106, 8013-8025,  
636 10.1029/2000jd900681, 2001.

637 Heard, D. E., and Pilling, M. J.: Measurement of OH and HO<sub>2</sub> in the troposphere, *Chemical Reviews*, 103, 5163-5198,  
638 10.1021/cr020522s, 2003.

639 Hofzumahaus, A., Aschmutat, U., Hessling, M., Holland, F., and Ehhalt, D. H.: The measurement of tropospheric OH radicals  
640 by laser-induced fluorescence spectroscopy during the POPCORN field campaign, *Geophysical Research Letters*, 23, 2541-  
641 2544, 10.1029/96gl02205, 1996.

642 Hofzumahaus, A., Rohrer, F., Lu, K., Bohn, B., Brauers, T., Chang, C.-C., Fuchs, H., Holland, F., Kita, K., Kondo, Y., Li, X.,  
643 Lou, S., Shao, M., Zeng, L., Wahner, A., and Zhang, Y.: Amplified Trace Gas Removal in the Troposphere, *Science*, 324, 1702-  
644 1704, 10.1126/science.1164566, 2009.

645 Holland, F., Hessling, M., and Hofzumahaus, A.: IN-SITU MEASUREMENT OF TROPOSPHERIC OH RADICALS BY  
646 LASER-INDUCED FLUORESCENCE - A DESCRIPTION OF THE KFA INSTRUMENT, *Journal of the Atmospheric  
647 Sciences*, 52, 3393-3401, 10.1175/1520-0469(1995)052<3393:ismoto>2.0.Co;2, 1995.

648 Huang, X.-F., Chen, D.-L., Lan, Z.-J., Feng, N., He, L.-Y., Yu, G.-H., and Luan, S.-J.: Characterization of organic aerosol in  
649 fine particles in a mega-city of South China: Molecular composition, seasonal variation, and size distribution, *Atmospheric  
650 Research*, 114-115, 28-37, <https://doi.org/10.1016/j.atmosres.2012.05.019>, 2012a.

651 Huang, X.-F., Sun, T.-L., Zeng, L.-W., Yu, G.-H., and Luan, S.-J.: Black carbon aerosol characterization in a coastal city in  
652 South China using a single particle soot photometer, *Atmospheric Environment*, 51, 21-28,  
653 <https://doi.org/10.1016/j.atmosenv.2012.01.056>, 2012b.

654 Jones, C. E., Hopkins, J. R., and Lewis, A. C.: In situ measurements of isoprene and monoterpenes within a south-east Asian  
655 tropical rainforest, *Atmospheric Chemistry and Physics*, 11, 6971-6984, 10.5194/acp-11-6971-2011, 2011.

656 Kanaya, Y., Sadanaga, Y., Matsumoto, J., Sharma, U. K., Hirokawa, J., Kajii, Y., and Akimoto, H.: Daytime HO<sub>2</sub> concentrations  
657 at Oki Island, Japan, in summer 1998: Comparison between measurement and theory, *Journal of Geophysical Research-  
658 Atmospheres*, 105, 24205-24222, 10.1029/2000jd900308, 2000.

659 Kanaya, Y., Cao, R., Kato, S., Miyakawa, Y., Kajii, Y., Tanimoto, H., Yokouchi, Y., Mochida, M., Kawamura, K., and Akimoto,  
660 H.: Chemistry of OH and HO<sub>2</sub> radicals observed at Rishiri Island, Japan, in September 2003: Missing daytime sink of HO<sub>2</sub>  
661 and positive nighttime correlations with monoterpenes, *Journal of Geophysical Research-Atmospheres*, 112,  
662 10.1029/2006jd007987, 2007.

663 Lelieveld, J., Butler, T. M., Crowley, J. N., Dillon, T. J., Fischer, H., Ganzeveld, L., Harder, H., Lawrence, M. G., Martinez,  
664 M., Taraborrelli, D., and Williams, J.: Atmospheric oxidation capacity sustained by a tropical forest, *Nature*, 452, 737-740,  
665 10.1038/nature06870, 2008.

666 Levy, H.: NORMAL ATMOSPHERE - LARGE RADICAL AND FORMALDEHYDE CONCENTRATIONS PREDICTED,  
667 *Science*, 173, 141-&, 10.1126/science.173.3992.141, 1971.

668 Li, K., Jacob, D. J., Liao, H., Shen, L., Zhang, Q., and Bates, K. H.: Anthropogenic drivers of 2013-2017 trends in summer  
669 surface ozone in China, *Proceedings of the National Academy of Sciences of the United States of America*, 116, 422-427,  
670 10.1073/pnas.1812168116, 2019.

671 Li, Z., Xue, L., Yang, X., Zha, Q., Tham, Y. J., Yan, C., Louie, P. K. K., Luk, C. W. Y., Wang, T., and Wang, W.: Oxidizing

672 capacity of the rural atmosphere in Hong Kong, Southern China, *Science of the Total Environment*, 612, 1114-1122,  
673 10.1016/j.scitotenv.2017.08.310, 2018.

674 Liu, S., Li, X., Shen, X., Zeng, L., Huang, X., Zhu, B., Lin, L., and Lou, S.: Measurement and partition analysis of atmospheric  
675 OH reactivity in autumn in Shenzhen, *Acta Scientiae Circumstantiae*, 39, 3600-3610, 2019.

676 Liu, Z., Wang, Y., Hu, B., Lu, K., Tang, G., Ji, D., Yang, X., Gao, W., Xie, Y., Liu, J., Yao, D., Yang, Y., and Zhang, Y.:  
677 Elucidating the quantitative characterization of atmospheric oxidation capacity in Beijing, China, *Science of the Total  
678 Environment*, 771, 10.1016/j.scitotenv.2021.145306, 2021.

679 Lou, S., Holland, F., Rohrer, F., Lu, K., Bohn, B., Brauers, T., Chang, C. C., Fuchs, H., Haeseler, R., Kita, K., Kondo, Y., Li,  
680 X., Shao, M., Zeng, L., Wahner, A., Zhang, Y., Wang, W., and Hofzumahaus, A.: Atmospheric OH reactivities in the Pearl  
681 River Delta - China in summer 2006: measurement and model results, *Atmospheric Chemistry and Physics*, 10, 11243-11260,  
682 10.5194/acp-10-11243-2010, 2010.

683 Lu, K., Guo, S., Tan, Z., Wang, H., Shang, D., Liu, Y., Li, X., Wu, Z., Hu, M., and Zhang, Y.: Exploring atmospheric free-  
684 radical chemistry in China: the self-cleansing capacity and the formation of secondary air pollution, *National Science Review*,  
685 6, 579-594, 10.1093/nsr/nwy073, 2019.

686 Lu, K. D., Rohrer, F., Holland, F., Fuchs, H., Bohn, B., Brauers, T., Chang, C. C., Haeseler, R., Hu, M., Kita, K., Kondo, Y.,  
687 Li, X., Lou, S. R., Nehr, S., Shao, M., Zeng, L. M., Wahner, A., Zhang, Y. H., and Hofzumahaus, A.: Observation and modelling  
688 of OH and HO<sub>2</sub> concentrations in the Pearl River Delta 2006: a missing OH source in a VOC rich atmosphere, *Atmospheric  
689 Chemistry and Physics*, 12, 1541-1569, 10.5194/acp-12-1541-2012, 2012.

690 Lu, K. D., Hofzumahaus, A., Holland, F., Bohn, B., Brauers, T., Fuchs, H., Hu, M., Haeseler, R., Kita, K., Kondo, Y., Li, X.,  
691 Lou, S. R., Oebel, A., Shao, M., Zeng, L. M., Wahner, A., Zhu, T., Zhang, Y. H., and Rohrer, F.: Missing OH source in a  
692 suburban environment near Beijing: observed and modelled OH and HO<sub>2</sub> concentrations in summer 2006, *Atmospheric  
693 Chemistry and Physics*, 13, 1057-1080, 10.5194/acp-13-1057-2013, 2013.

694 Ma, X., Tan, Z., Lu, K., Yang, X., Liu, Y., Li, S., Li, X., Chen, S., Novelli, A., Cho, C., Zeng, L., Wahner, A., and Zhang, Y.:  
695 Winter photochemistry in Beijing: Observation and model simulation of OH and HO<sub>2</sub> radicals at an urban site, *Science of the  
696 Total Environment*, 685, 85-95, 10.1016/j.scitotenv.2019.05.329, 2019a.

697 Ma, X., Tan, Z., Lu, K., Yang, X., Chen, X., Wang, H., Chen, S., Fang, X., Li, S., Li, X., Liu, J., Liu, Y., Lou, S., Qiu, W.,  
698 Wang, H., Zeng, L., and Zhang, Y.: OH and HO<sub>2</sub> radical chemistry at a suburban site during the EXPLORE-YRD campaign  
699 in 2018, *Atmospheric Chemistry and Physics*, 22, 7005-7028, 10.5194/acp-22-7005-2022, 2022a.

700 Ma, X. F., Tan, Z. F., Lu, K. D., Yang, X. P., Chen, X. R., Wang, H. C., Chen, S. Y., Fang, X., Li, S. L., Li, X., Liu, J. W., Liu,  
701 Y., Lou, S. R., Qiu, W. Y., Wang, H. L., Zeng, L. M., and Zhang, Y. H.: OH and HO<sub>2</sub> radical chemistry at a suburban site during  
702 the EXPLORE-YRD campaign in 2018, *Atmospheric Chemistry and Physics*, 22, 7005-7028, 10.5194/acp-22-7005-2022,  
703 2022b.

704 Ma, X. Y., Jia, H. L., Sha, T., An, J. L., and Tian, R.: Spatial and seasonal characteristics of particulate matter and gaseous  
705 pollution in China: Implications for control policy, *Environmental Pollution*, 248, 421-428, 10.1016/j.envpol.2019.02.038,  
706 2019b.

707 Mao, J., Jacob, D. J., Evans, M. J., Olson, J. R., Ren, X., Brune, W. H., St Clair, J. M., Crounse, J. D., Spencer, K. M., Beaver,  
708 M. R., Wennberg, P. O., Cubison, M. J., Jimenez, J. L., Fried, A., Weibring, P., Walega, J. G., Hall, S. R., Weinheimer, A. J.,  
709 Cohen, R. C., Chen, G., Crawford, J. H., McNaughton, C., Clarke, A. D., Jaegle, L., Fisher, J. A., Yantosca, R. M., Le Sager,  
710 P., and Carouge, C.: Chemistry of hydrogen oxide radicals (HO<sub>x</sub>) in the Arctic troposphere in spring, *Atmospheric Chemistry  
711 and Physics*, 10, 5823-5838, 10.5194/acp-10-5823-2010, 2010.

712 Mao, J., Ren, X., Zhang, L., Van Duin, D. M., Cohen, R. C., Park, J. H., Goldstein, A. H., Paulot, F., Beaver, M. R., Crounse,  
713 J. D., Wennberg, P. O., DiGangi, J. P., Henry, S. B., Keutsch, F. N., Park, C., Schade, G. W., Wolfe, G. M., Thornton, J. A., and  
714 Brune, W. H.: Insights into hydroxyl measurements and atmospheric oxidation in a California forest, *Atmospheric Chemistry  
715 and Physics*, 12, 8009-8020, 10.5194/acp-12-8009-2012, 2012.

716 Novelli, A., Hens, K., Ernest, C. T., Kubistin, D., Regelin, E., Elste, T., Plass-Duelmer, C., Martinez, M., Lelieveld, J., and  
717 Harder, H.: Characterisation of an inlet pre-injector laser-induced fluorescence instrument for the measurement of atmospheric  
718 hydroxyl radicals, *Atmospheric Measurement Techniques*, 7, 3413-3430, 10.5194/amt-7-3413-2014, 2014.

719 Peeters, J., Nguyen, T. L., and Vereecken, L.: HOx radical regeneration in the oxidation of isoprene, *Physical Chemistry*  
720 *Chemical Physics*, 11, 5935-5939, 10.1039/b908511d, 2009.

721 Peeters, J., and Muller, J.-F.: HOx radical regeneration in isoprene oxidation via peroxy radical isomerisations. II: experimental  
722 evidence and global impact, *Physical Chemistry Chemical Physics*, 12, 14227-14235, 10.1039/c0cp00811g, 2010.

723 Peeters, J., Muller, J.-F., Stavrou, T., and Vinh Son, N.: Hydroxyl Radical Recycling in Isoprene Oxidation Driven by  
724 Hydrogen Bonding and Hydrogen Tunneling: The Upgraded LIM1 Mechanism, *Journal of Physical Chemistry A*, 118, 8625-  
725 8643, 10.1021/jp5033146, 2014.

726 Ren, X., Olson, J. R., Crawford, J. H., Brune, W. H., Mao, J., Long, R. B., Chen, Z., Chen, G., Avery, M. A., Sachse, G. W.,  
727 Barrick, J. D., Diskin, G. S., Huey, L. G., Fried, A., Cohen, R. C., Heikes, B., Wennberg, P. O., Singh, H. B., Blake, D. R., and  
728 Shetter, R. E.: HOx chemistry during INTEX-A 2004: Observation, model calculation, and comparison with previous studies,  
729 *Journal of Geophysical Research-Atmospheres*, 113, 10.1029/2007jd009166, 2008.

730 Shu, L., Wang, T. J., Han, H., Xie, M., Chen, P. L., Li, M. M., and Wu, H.: Summertime ozone pollution in the Yangtze River  
731 Delta of eastern China during 2013-2017: Synoptic impacts and source apportionment, *Environmental Pollution*, 257,  
732 10.1016/j.envpol.2019.113631, 2020.

733 Song, H., Zou, Q., and Lu, K.: Parameterization and Application of Hydroperoxyl Radicals (HO<sub>2</sub>) Heterogeneous Uptake  
734 Coefficient, *Progress in Chemistry*, 33, 1161-1173, 10.7536/pc200749, 2021.

735 Song, H., Lu, K., Dong, H., Tan, Z., Chen, S., Zeng, L., and Zhang, Y.: Reduced Aerosol Uptake of Hydroperoxyl Radical May  
736 Increase the Sensitivity of Ozone Production to Volatile Organic Compounds, *Environmental Science & Technology Letters*,  
737 9, 22-29, 10.1021/acs.estlett.1c00893, 2022.

738 Stevens, P. S., Mather, J. H., Brune, W. H., Eisele, F., Tanner, D., Jefferson, A., Cantrell, C., Shetter, R., Sewall, S., Fried, A.,  
739 Henry, B., Williams, E., Baumann, K., Goldan, P., and Kuster, W.: HO<sub>2</sub>/OH and RO(2)/HO<sub>2</sub> ratios during the Tropospheric  
740 OH Photochemistry Experiment: Measurement and theory, *Journal of Geophysical Research-Atmospheres*, 102, 6379-6391,  
741 10.1029/96jd01704, 1997.

742 Stone, D., Whalley, L. K., and Heard, D. E.: Tropospheric OH and HO<sub>2</sub> radicals: field measurements and model comparisons,  
743 *Chemical Society Reviews*, 41, 6348-6404, 10.1039/c2cs35140d, 2012.

744 Stone, D., Evans, M. J., Walker, H., Ingham, T., Vaughan, S., Ouyang, B., Kennedy, O. J., McLeod, M. W., Jones, R. L.,  
745 Hopkins, J., Punjabi, S., Lidster, R., Hamilton, J. F., Lee, J. D., Lewis, A. C., Carpenter, L. J., Forster, G., Oram, D. E., Reeves,  
746 C. E., Bauguitte, S., Morgan, W., Coe, H., Aruffo, E., Dari-Salisburgo, C., Giammaria, F., Di Carlo, P., and Heard, D. E.:  
747 Radical chemistry at night: comparisons between observed and modelled HOx, NO<sub>3</sub> and N<sub>2</sub>O<sub>5</sub> during the RONOCO project,  
748 *Atmospheric Chemistry and Physics*, 14, 1299-1321, 10.5194/acp-14-1299-2014, 2014.

749 Taketani, F., Kanaya, Y., Pochanart, P., Liu, Y., Li, J., Okuzawa, K., Kawamura, K., Wang, Z., and Akimoto, H.: Measurement  
750 of overall uptake coefficients for HO<sub>2</sub> radicals by aerosol particles sampled from ambient air at Mts. Tai and Mang (China),  
751 *Atmospheric Chemistry and Physics*, 12, 11907-11916, 10.5194/acp-12-11907-2012, 2012.

752 Tan, Z., Fuchs, H., Lu, K., Hofzumahaus, A., Bohn, B., Broch, S., Dong, H., Gomm, S., Haeseler, R., He, L., Holland, F., Li,  
753 X., Liu, Y., Lu, S., Rohrer, F., Shao, M., Wang, B., Wang, M., Wu, Y., Zeng, L., Zhang, Y., Wahner, A., and Zhang, Y.: Radical  
754 chemistry at a rural site (Wangdu) in the North China Plain: observation and model calculations of OH, HO<sub>2</sub> and RO<sub>2</sub> radicals,  
755 *Atmospheric Chemistry and Physics*, 17, 663-690, 10.5194/acp-17-663-2017, 2017.

756 Tan, Z., Rohrer, F., Lu, K., Ma, X., Bohn, B., Broch, S., Dong, H., Fuchs, H., Gkatzelis, G. I., Hofzumahaus, A., Holland, F.,  
757 Li, X., Liu, Y., Liu, Y., Novelli, A., Shao, M., Wang, H., Wu, Y., Zeng, L., Hu, M., Kiendler-Scharr, A., Wahner, A., and Zhang,  
758 Y.: Wintertime photochemistry in Beijing: observations of ROx radical concentrations in the North China Plain during the  
759 BEST-ONE campaign, *Atmospheric Chemistry and Physics*, 18, 12391-12411, 10.5194/acp-18-12391-2018, 2018.

760 Tan, Z., Lu, K., Hofzumahaus, A., Fuchs, H., Bohn, B., Holland, F., Liu, Y., Rohrer, F., Shao, M., Sun, K., Wu, Y., Zeng, L.,  
761 Zhang, Y., Zou, Q., Kiendler-Scharr, A., Wahner, A., and Zhang, Y.: Experimental budgets of OH, HO<sub>2</sub>, and RO<sub>2</sub> radicals and  
762 implications for ozone formation in the Pearl River Delta in China 2014, *Atmospheric Chemistry and Physics*, 19, 7129-7150,  
763 10.5194/acp-19-7129-2019, 2019.

764 Tan, Z., Hofzumahaus, A., Lu, K., Brown, S. S., Holland, F., Huey, L. G., Kiendler-Scharr, A., Li, X., Liu, X., Ma, N., Min,  
765 K.-E., Rohrer, F., Shao, M., Wahner, A., Wang, Y., Wiedensohler, A., Wu, Y., Wu, Z., Zeng, L., Zhang, Y., and Fuchs, H.: No

766 Evidence for a Significant Impact of Heterogeneous Chemistry on Radical Concentrations in the North China Plain in Summer  
767 2014, *Environmental Science & Technology*, 54, 5973-5979, 10.1021/acs.est.0c00525, 2020.

768 Tan, Z., Ma, X., Lu, K., Jiang, M., Zou, Q., Wang, H., Zeng, L., and Zhang, Y.: Direct evidence of local photochemical  
769 production driven ozone episode in Beijing: A case study, *Science of the Total Environment*, 800,  
770 10.1016/j.scitotenv.2021.148868, 2021.

771 Wang, T., Xue, L. K., Brimblecombe, P., Lam, Y. F., Li, L., and Zhang, L.: Ozone pollution in China: A review of concentrations,  
772 meteorological influences, chemical precursors, and effects, *Science of the Total Environment*, 575, 1582-1596,  
773 10.1016/j.scitotenv.2016.10.081, 2017a.

774 Wang, W., Parrish, D. D., Li, X., Shao, M., Liu, Y., Mo, Z., Lu, S., Hu, M., Fang, X., Wu, Y., Zeng, L., and Zhang, Y.: Exploring  
775 the drivers of the increased ozone production in Beijing in summertime during 2005-2016, *Atmospheric Chemistry and Physics*,  
776 20, 15617-15633, 10.5194/acp-20-15617-2020, 2020.

777 Wang, X., Wang, H., Xue, L., Wang, T., Wang, L., Gu, R., Wang, W., Tham, Y. J., Wang, Z., Yang, L., Chen, J., and Wang, W.:  
778 Observations of N<sub>2</sub>O<sub>5</sub> and ClNO<sub>2</sub> at a polluted urban surface site in North China: High N<sub>2</sub>O<sub>5</sub> uptake coefficients and low  
779 ClNO<sub>2</sub> product yields, *Atmospheric Environment*, 156, 125-134, 10.1016/j.atmosenv.2017.02.035, 2017b.

780 Whalley, L. K., Edwards, P. M., Furneaux, K. L., Goddard, A., Ingham, T., Evans, M. J., Stone, D., Hopkins, J. R., Jones, C.  
781 E., Karunaharan, A., Lee, J. D., Lewis, A. C., Monks, P. S., Moller, S. J., and Heard, D. E.: Quantifying the magnitude of a  
782 missing hydroxyl radical source in a tropical rainforest, *Atmospheric Chemistry and Physics*, 11, 7223-7233, 10.5194/acp-11-  
783 7223-2011, 2011.

784 Whalley, L. K., Stone, D., George, I. J., Mertes, S., van Pinxteren, D., Tilgner, A., Herrmann, H., Evans, M. J., and Heard, D.  
785 E.: The influence of clouds on radical concentrations: observations and modelling studies of HO<sub>x</sub> during the Hill Cap Cloud  
786 Thuringia (HCCT) campaign in 2010, *Atmospheric Chemistry and Physics*, 15, 3289-3301, 10.5194/acp-15-3289-2015, 2015.

787 Whalley, L. K., Slater, E. J., Woodward-Massey, R., Ye, C., Lee, J. D., Squires, F., Hopkins, J. R., Dunmore, R. E., Shaw, M.,  
788 Hamilton, J. F., Lewis, A. C., Mehra, A., Worrall, S. D., Bacak, A., Bannan, T. J., Coe, H., Percival, C. J., Ouyang, B., Jones,  
789 R. L., Crilley, L. R., Kramer, L. J., Bloss, W. J., Vu, T., Kotthaus, S., Grimmond, S., Sun, Y., Xu, W., Yue, S., Ren, L., Acton,  
790 W. J. F., Hewitt, C. N., Wang, X., Fu, P., and Heard, D. E.: Evaluating the sensitivity of radical chemistry and ozone formation  
791 to ambient VOCs and NO<sub>x</sub> in Beijing, *Atmospheric Chemistry and Physics*, 21, 2125-2147, 10.5194/acp-21-2125-2021, 2021.

792 Xue, L., Gu, R., Wang, T., Wang, X., Saunders, S., Blake, D., Louie, P. K. K., Luk, C. W. Y., Simpson, I., Xu, Z., Wang, Z.,  
793 Gao, Y., Lee, S., Mellouki, A., and Wang, W.: Oxidative capacity and radical chemistry in the polluted atmosphere of Hong  
794 Kong and Pearl River Delta region: analysis of a severe photochemical smog episode, *Atmospheric Chemistry and Physics*,  
795 16, 9891-9903, 10.5194/acp-16-9891-2016, 2016.

796 Yang, X., Wang, H., Tan, Z., Lu, K., and Zhang, Y.: Observations of OH Radical Reactivity in Field Studies, *Acta Chimica*  
797 *Sinica*, 77, 613-624, 10.6023/a19030094, 2019.

798 Yang, X., Lu, K., Ma, X., Liu, Y., Wang, H., Hu, R., Li, X., Lou, S., Chen, S., Dong, H., Wang, F., Wang, Y., Zhang, G., Li, S.,  
799 Yang, S., Yang, Y., Kuang, C., Tan, Z., Chen, X., Qiu, P., Zeng, L., Xie, P., and Zhang, Y.: Observations and modeling of OH  
800 and HO<sub>2</sub> radicals in Chengdu, China in summer 2019, *The Science of the total environment*, 772, 144829-144829,  
801 10.1016/j.scitotenv.2020.144829, 2021.

802 Yang, Y., Wang, Y., Yao, D., Zhao, S., Yang, S., Ji, D., Sun, J., Wang, Y., Liu, Z., Hu, B., Zhang, R., and Wang, Y.: Significant  
803 decreases in the volatile organic compound concentration, atmospheric oxidation capacity and photochemical reactivity during  
804 the National Day holiday over a suburban site in the North China Plain, *Environmental Pollution*, 263,  
805 10.1016/j.envpol.2020.114657, 2020a.

806 Yang, Y., Wang, Y., Yao, D., Zhao, S., Yang, S., Ji, D., Sun, J., Wang, Y., Liu, Z., Hu, B., Zhang, R., and Wang, Y.: Significant  
807 decreases in the volatile organic compound concentration, atmospheric oxidation capacity and photochemical reactivity during  
808 the National Day holiday over a suburban site in the North China Plain, *Environmental Pollution*, 263, 114657,  
809 <https://doi.org/10.1016/j.envpol.2020.114657>, 2020b.

810 Yu, D., Tan, Z., Lu, K., Ma, X., Li, X., Chen, S., Zhu, B., Lin, L., Li, Y., Qiu, P., Yang, X., Liu, Y., Wang, H., He, L., Huang,  
811 X., and Zhang, Y.: An explicit study of local ozone budget and NO<sub>x</sub>-VOCs sensitivity in Shenzhen China, *Atmospheric*  
812 *Environment*, 224, 117304, <https://doi.org/10.1016/j.atmosenv.2020.117304>, 2020.

813 Zhang, Y. H., Hu, M., Zhong, L. J., Wiedensohler, A., Liu, S. C., Andreae, M. O., Wang, W., and Fan, S. J.: Regional Integrated  
814 Experiments on Air Quality over Pearl River Delta 2004 (PRIDE-PRD2004): Overview, *Atmospheric Environment*, 42, 6157-  
815 6173, 10.1016/j.atmosenv.2008.03.025, 2008.

816 Zhou, J., Murano, K., Kohno, N., Sakamoto, Y., and Kajii, Y.: Real-time quantification of the total HO<sub>2</sub> reactivity of ambient  
817 air and HO<sub>2</sub> uptake kinetics onto ambient aerosols in Kyoto (Japan), *Atmospheric Environment*, 223,  
818 10.1016/j.atmosenv.2020.117189, 2020.

819 Zhou, J., Sato, K., Bai, Y., Fukusaki, Y., Kousa, Y., Ramasamy, S., Takami, A., Yoshino, A., Nakayama, T., Sadanaga, Y.,  
820 Nakashima, Y., Li, J., Murano, K., Kohno, N., Sakamoto, Y., and Kajii, Y.: Kinetics and impacting factors of HO<sub>2</sub> uptake onto  
821 submicron atmospheric aerosols during the 2019 Air QUALity Study (AQUAS) in Yokohama, Japan, *Atmospheric Chemistry  
822 and Physics*, 21, 12243-12260, 10.5194/acp-21-12243-2021, 2021.

823 Zhu, J., Wang, S., Wang, H., Jing, S., Lou, S., Saiz-Lopez, A., and Zhou, B.: Observationally constrained modeling of  
824 atmospheric oxidation capacity and photochemical reactivity in Shanghai, China, *Atmospheric Chemistry and Physics*, 20,  
825 1217-1232, 10.5194/acp-20-1217-2020, 2020.

826